Numerical analysis of a parallel triple-jet of liquid-sodium in a turbulent forced convection regime

Cascioli, E.; Kaaks, B.; Keijers, S.; Van Tichelen, K.; Kenjereš, S.

DOI
10.1016/j.icheatmasstransfer.2024.107696

Publication date
2024

Document Version
Final published version

Published in
International Communications in Heat and Mass Transfer

International Communications in Heat and Mass Transfer 156 (2024) 107696

Contents lists available at ScienceDirect

International Communications in Heat and Mass Transfer

journal homepage: www.elsevier.com/locate/ichmt

Numerical analysis of a parallel triple-jet of liquid-sodium in a turbulent forced convection regime

E. Cascioli [a,b], B. Kaaks [a], S. Keijers [b], K. Van Tichelen [b], S. Kenjereš [a,*]

[a] Delft University of Technology, Faculty of Applied Sciences, Department of Chemical Engineering and J. M. Burgerscentrum Research School for Fluid Mechanics, Van der Maasweg 9, 2629 HZ Delft, the Netherlands
[b] SCK-CEN, Belgian Nuclear Research Centre, Boeretang 200, 2400 Mol, Belgium

ARTICLE INFO

Keywords:
Turbulent forced convection
Liquid metal
Triple-jet mixing and heat transfer
Small modular nuclear reactors
Combined dynamic LES/DNS
T-RANS

ABSTRACT

In the present study, we have applied a combined wall-resolving dynamic Large-Eddy Simulation (LES) (for the velocity field) and Direct Numerical Simulation (DNS) (for the temperature field) approach for mixing of parallel triple-jets with different temperatures of liquid sodium in a turbulent forced convection regime. Because of the high thermal conductivity of sodium (a low-Prandtl fluid), we adopted the dynamic Smagorinsky subgrid closure for the unresolved velocity scales, while the thermal scales are fully resolved. Furthermore, the Time-dependent Reynolds-Averaged Navier-Stokes (T-RANS) approach with the high-Reynolds number variant (i.e. with the wall functions as boundary conditions along solid boundaries) of the four-equation eddy viscosity model ($k-\varepsilon-k_\theta-\varepsilon_\theta$) was applied. The fine-mesh LES/DNS provided a close agreement with the experimental data for both velocity and temperature fields (for both first- and second-moments). In contrast, the coarse-mesh LES/DNS overestimated the turbulent kinetic energy profiles at different distances from the inlet plane. The T-RANS results confirmed a good agreement with the mean streamwise velocity and turbulent kinetic energy, as well as the mean temperature profiles. Finally, the analysis of power spectral density distributions of the temperature signal revealed that all simulation techniques captured a dominant flow frequency originating from the induced Kelvin-Helmholtz instabilities between the side and central jets. The presented combined dynamic LES/DNS approach is recommended for future simulations of the turbulent forced convection flows of low Prandtl fluids, especially if thermal fatigue effects need to be predicted correctly.

1. Introduction

During the last decade, we have witnessed a renewed interest in liquid metal-cooled fast nuclear reactors in the market, particularly with regard to the small modular reactor technology, Triplett et al. [1], Soloviev et al. [2], etc. Moreover, other projects on advanced pool-type reactors cooled by liquid metals were already launched, such as the Multi-Purpose hYbrid Research Reactor for High-tech Applications (MYRRHA) by the Belgian Nuclear Research Centre (SCK-CEN), Van Tichelen et al. [3]. For example, considering the MYRRHA reactor, we can recognize that turbulent mixing phenomena also occur in quasi-unconfined regions, namely the upper and lower plena. Similarly to the wall-confined flows, it is important to properly understand the thermal hydraulics phenomena to reliably predict velocity and temperature fields in these regions too. For this purpose, Computational Fluid Dynamics (CFD) is extensively used to support both safety analysis and design process, as well as for the prediction, control and optimization of the normal and accidental operational conditions. Turbulent Heat Transfer (THT) modeling for liquid metals requires a re-evaluation of the Reynolds analogy, which is normally employed in the case of Reynolds Averaged Navier-Stokes (RANS) simulations when the fluid Prandtl number (Pr) is close to the unity. It is known that such a standard approach does not work for turbulent flow regimes of liquid metals, where $Pr \ll 1$, Grötzbach [4]. In literature, a more advanced THT models have been proposed for low-Pr fluids in the wall-bounded geometries, e.g. Shams et al. [5], Roelofs et al. [6]. The early modeling approach of Kays [7] proposed a redefinition of the turbulent Prandtl number (Pr_t) correlation to include the low-Pr effects. More advanced models proposed solving additional PDEs for the thermal field turbulence, which include the transport equations for temperature variance and its dissipation rate (so-called four-equation ($k-\varepsilon-k_\theta-\epsilon_\theta$) model), for the forced- and natural-convection cases (e.g. Abe et al. [8] and Hanjalić et al. [9], respectively). This class of turbulence models was employed

* Corresponding author.
E-mail address: s.kenjeres@tudelft.nl (S. Kenjereš).

https://doi.org/10.1016/j.icheatmasstransfer.2024.107696

Available online 16 June 2024

Nomenclature

C_s	Smagorinsky coefficient (−)
f_0	characteristic frequency (1/s)
k	turbulence kinetic energy (m^2/s^2)
k_θ	temperature variance (K^2)
p	pressure (Pa)
T	temperature (K)
U_i	velocity vector (m/s)

Greek symbols

α	thermal diffusion (m^2/s)
ν	kinematic viscosity (m^2/s)
ν_t	turbulent viscosity (m^2/s)
ν_{SGS}	subgrid viscosity (m^2/s)
ρ	density (kg/m^3)
τ_{ij}	subgrid turbulence stress tensor (m^2/s^2)
ε	dissipation rate of turbulence kinetic energy (m^2/s^3)
ε_θ	dissipation rate of temperature variance (K^2/s)

Other symbols and Abbreviations

DFT	Discrete Fourier Transform
DNS	Direct Numerical Simulation
FTT	Flow Through Time (s)
LES	Large Eddy Simulation
Pr	Prandtl number (−)
PSD	Power Spectra Density
Re	Reynolds number (−)
Ri	Richardson number (−)
T-RANS	Time-dependent Reynolds-Averaged Navier-Stokes
THT	Turbulent Heat Transfer

Subscripts

C	cold
H	hot
J	jet
i,j	vector index

Table 1
Model coefficients of the $k-\varepsilon$ turbulence model.

C_μ	C_{ε_1}	C_{ε_2}	σ_k	σ_ε
0.09	1.44	1.92	1	1.3

Table 2
Model coefficients of the $k_\theta-\varepsilon_\theta$ heat transfer model.

C_θ	C_{p_1}	C_{p_2}	C_{d_1}	C_{d_2}	σ_{k_θ}	$\sigma_{\varepsilon_\theta}$
0.1	0.95	0.925	1	0.9	1.4	1.4

within the nuclear engineering community by Manservisi and Menghini [10,11], *Da* Viá et al. [12], Cascioli et al. [13]. At a higher modeling level, departing from the geometry-dependency and calibration optimization, algebraic heat flux THT models have been proposed and improved. The test cases for validation of such advanced THT models were mainly channel and pipe flows, backward-facing step and impinging jet flows, e.g. *Da* Viá et al. [12], De Santis and Shams [14], De Santis et al. [15], respectively. However, the turbulent mixing in larger regions of the reactor cannot be represented by such simple wall-confined flow configurations. In these reactor regions, the multiple-jets mixing is identified as a fundamental test case that needs to be investigated in detail. The experimental and numerical databases on turbulent jet flows with low-*Pr* fluids are rather limited in literature, as well as the related testing and development of low-*Pr* THT models.

The present study aims to provide a database based on the high-fidelity numerical simulations of the non-isothermal turbulent triple-

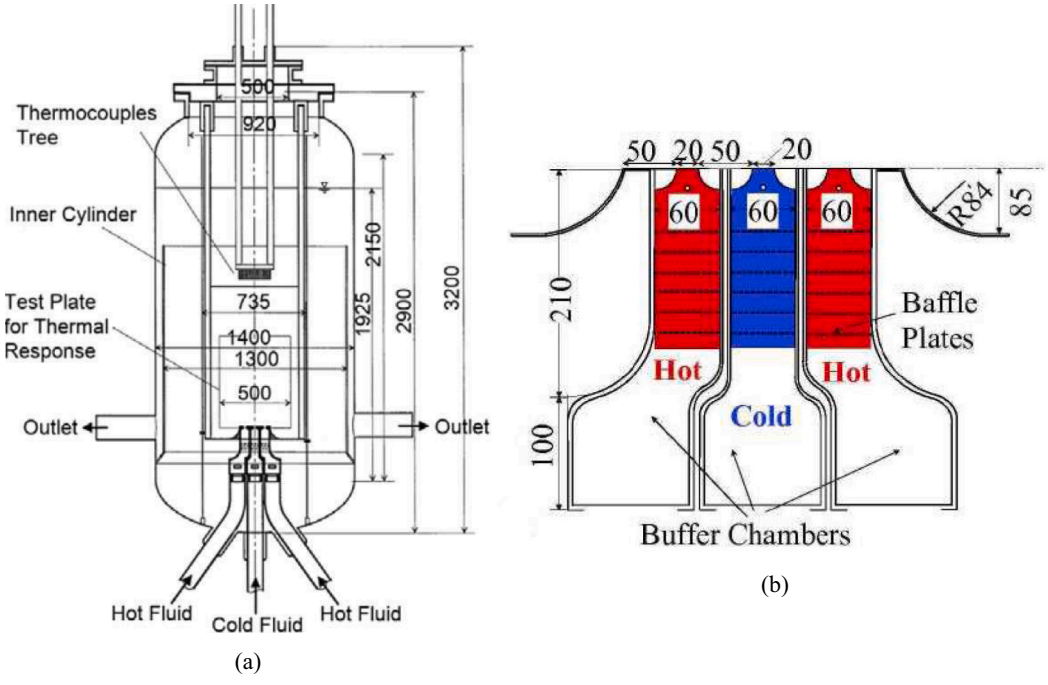

Fig. 1. Sketch of the experimental setup (a) and details of the inlet plane and nozzles (b), Kimura et al. [17,18].

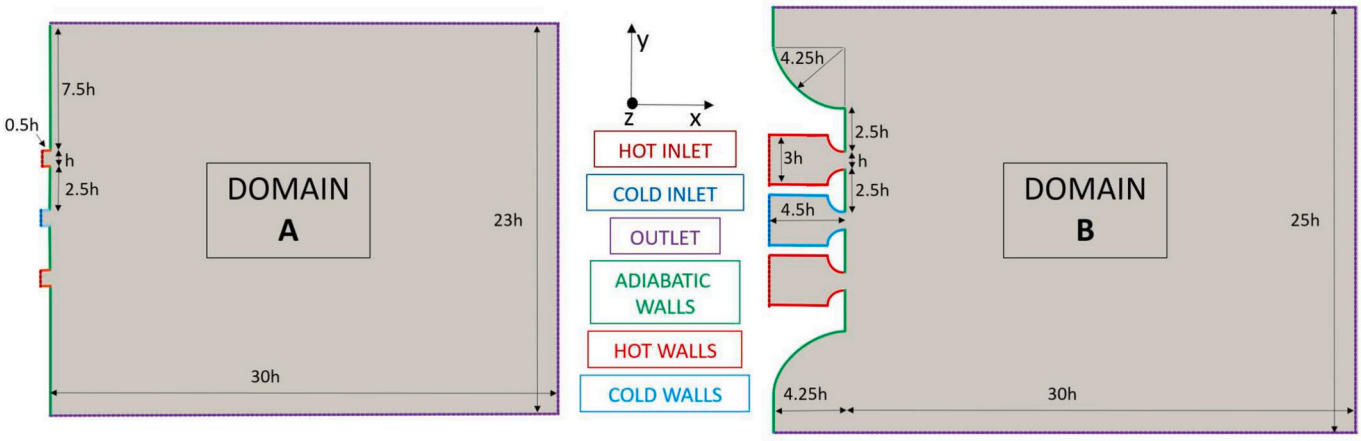

Fig. 2. Sketch of the computational domain A for the LES/DNSs and domain B for the T-RANS simulation. The spanwise extension (in the z-direction) of the computational domain is 5 h. Note that the various boundary conditions are indicated with different colors. The interior of domain A covers a volume of Lx : Ly : Lz = 0.6 : 0.46 : 0.1 m^3, whereas the interior of the domain B covers a volume of Lx : Ly : Lz = 0.6 : 0.5 : 0.1 m^3, respectively.

Table 3
Mesh details of the mixing region (no inlet channels).

Case	Domain	Millions of cells	$N_x \times N_y \times N_z$	$l_x \times l_y \times l_z$ [mm]
c-LES	A	2.0	240 × 166 × 50	2.5 × 2.8 × 2.0
f-LES	A	16	480 × 332 × 100	1.3 × 1.4 × 1.0
T-RANS	B	1.2	306 × 362 × 11	2.0 × 1.4 × 9.1

jet flow, which can be used for further development, testing, and validation of the new generation of the four-equation low-*Pr* turbulence models. The present contribution can be seen as an extension of our previous studies where we provided new sets of experimental and numerical databases for a single planar jet configuration in a highly turbulent forced convection regime over a range of low-Prandtl fluids ($0.006 \leq Pr \leq 0.71$), as presented in Cascioli et al. [13,16]. Here, we are considering the PLAner triple parallel JEts Sodium experimenT (PLAJEST) with sodium ($Pr = 0.006$) of the Japanese Atomic Energy Agency (JAEA), which was experimentally studied by Kimura et al. [17,18], and proposed as a benchmark validation study by Kobayashi et al. [19]. This configuration is characterized by a cold central jet and two hot side jets, which could be seen as a representative mixing condition within the upper plenum of the reactor.

The numerical results for this experimental configuration are relatively scarce in the literature. Tenchine et al. [20] performed a Large-Eddy Simulation (LES) approach with WALE (Wall Adapting Local Eddy viscosity) subgrid closure of Nicoud et al. [21] on a relatively coarse numerical mesh (containing approximately $5{\cdot}10^6$ tetrahedral unstructured elements within the fluid domain). Furthermore, the standard wall functions were employed along the different walls. The obtained results were in relatively good agreement with the measurements. More recently, Angeli [22] performed a systematic sensitivity analysis of various subgrid closures (SGS), numerical mesh resolution, and numerical schemes, mostly focusing on the velocity field of the PLAJEST experiment. It was found that the WALE subgrid closure performed better than the standard Smagorinsky, which was slightly too diffusive - especially on the too-coarse numerical mesh. In conclusion, it is recommended that additional numerical studies on even finer numerical meshes need to be performed to obtain a better distinction between the numerical viscosity and subgrid-scale contributions.

Motivated by these previous numerical studies, we present results of a high-fidelity LES / DNS approach (where dynamic subgrid closure is used for the transport of momentum (LES), and a fully numerically resolving transport of the heat (DNS)) for the PLAJEST test case. We also performed additional Time-dependent RANS (T-RANS) simulations employing the four-equation ($k-\varepsilon-k_\theta-\varepsilon_\theta$) model, which does not require a priori specification of Pr_t. The rationale behind the T-RANS

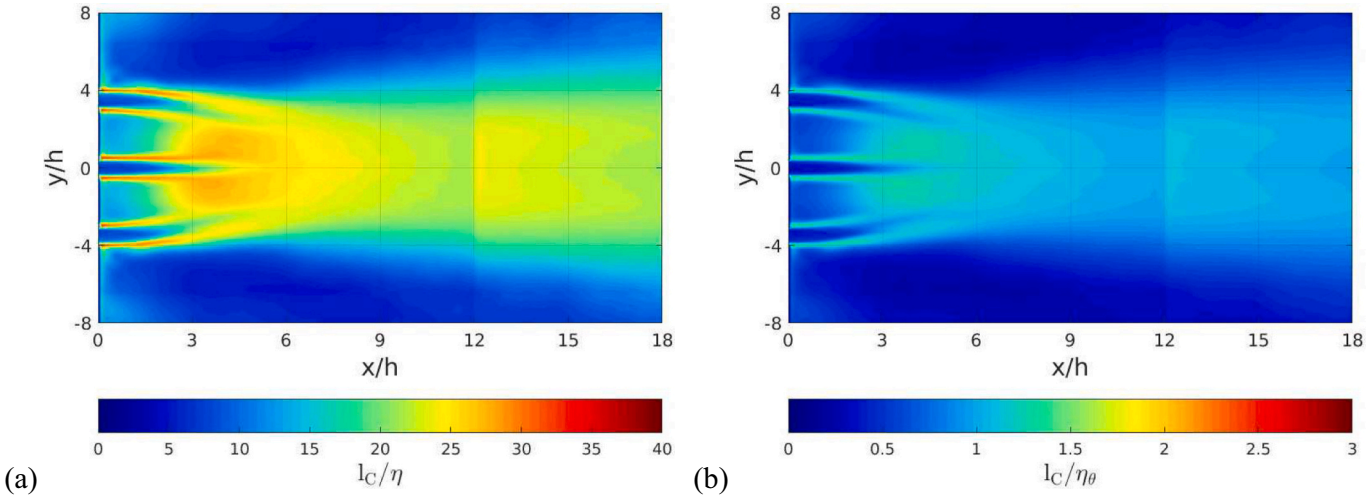

Fig. 3. Contours of characteristic computational cell length to smallest velocity (Kolmogorov) (l_c/η (a) and thermal (Corrsin) (l_c/η_θ) (b) scales ratio evaluated from the coarse LES/DNS.

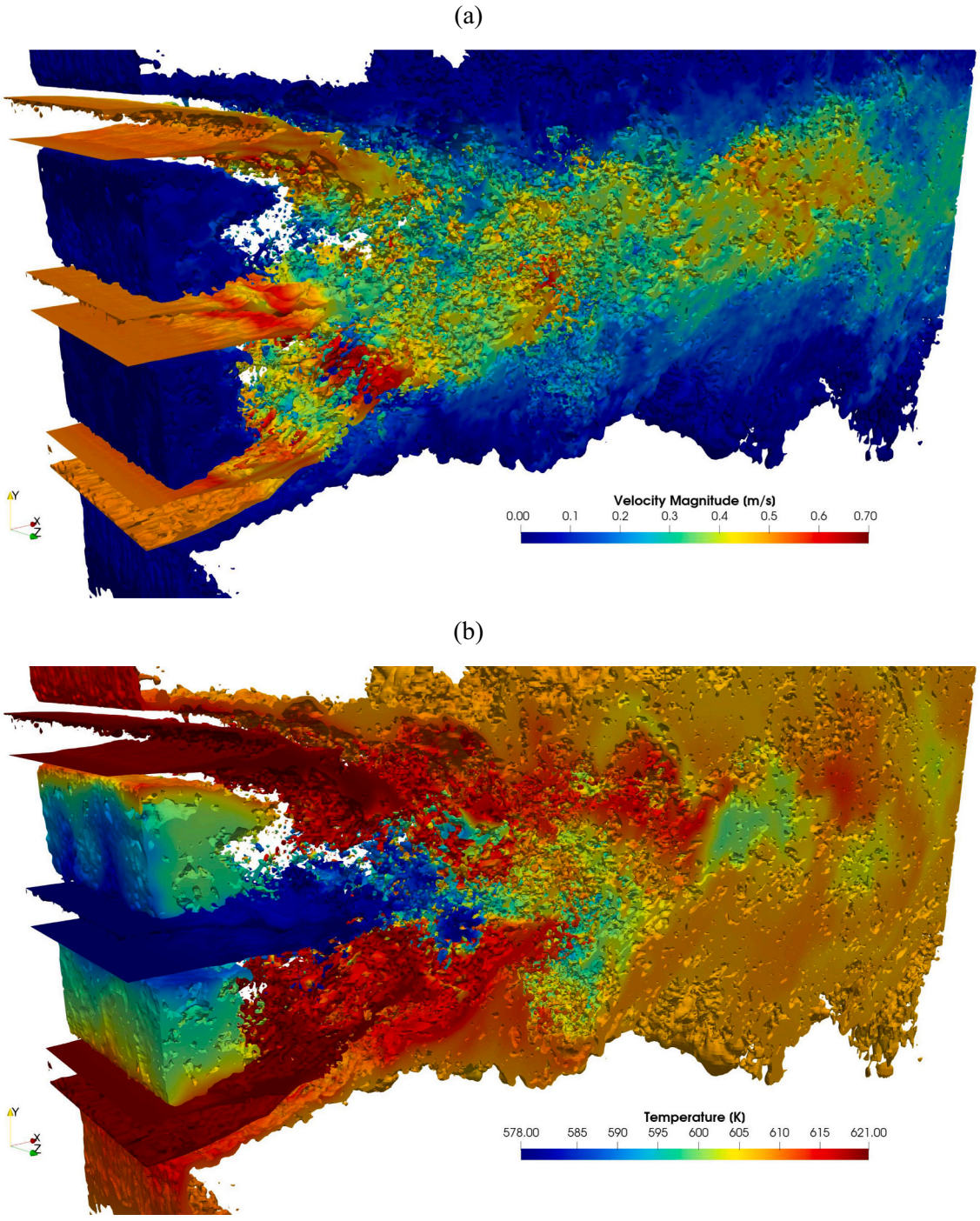

Fig. 4. Isovolumes of the instantaneous vorticity magnitude (15–45 Hz) colored by instantaneous velocity magnitude (a) and temperature (b) - data extracted from a fine mesh LES/DNS.

approach is in its significantly less intensive computational requirements in comparison to LES, both in terms of the requested numerical mesh size as well as in terms of the time integration (larger time steps and a shorter time-averaging procedure), Kenjereš and Hanjalić [23–25]. In addition to instantaneous fields and averaged first- and second-order statistics, we performed Power Spectral Density (PSD) analyses to assess the potential of T-RANS simulations in capturing dominant frequency peaks and dissipation regimes. The correct prediction of this information plays a crucial role to prevent and properly design the system against mechanical failure of the wall materials subject to thermal fatigue (thermal striping), as addressed in Nishimura et al. [26].

2. Numerical method

2.1. Governing equations

The fundamental conservation of mass, momentum, and energy can be described by the following equations:

$$\frac{\partial \widehat{U}_i}{\partial x_i} = 0 \tag{1}$$

$$\frac{\partial \widehat{U}_i}{\partial t} + \frac{\partial \widehat{U}_i \widehat{U}_j}{\partial x_j} = -\frac{1}{\rho}\frac{\partial \widehat{p}}{\partial x_i} + \nu \frac{\partial^2 \widehat{U}_i}{\partial x_j{}^2} \tag{2}$$

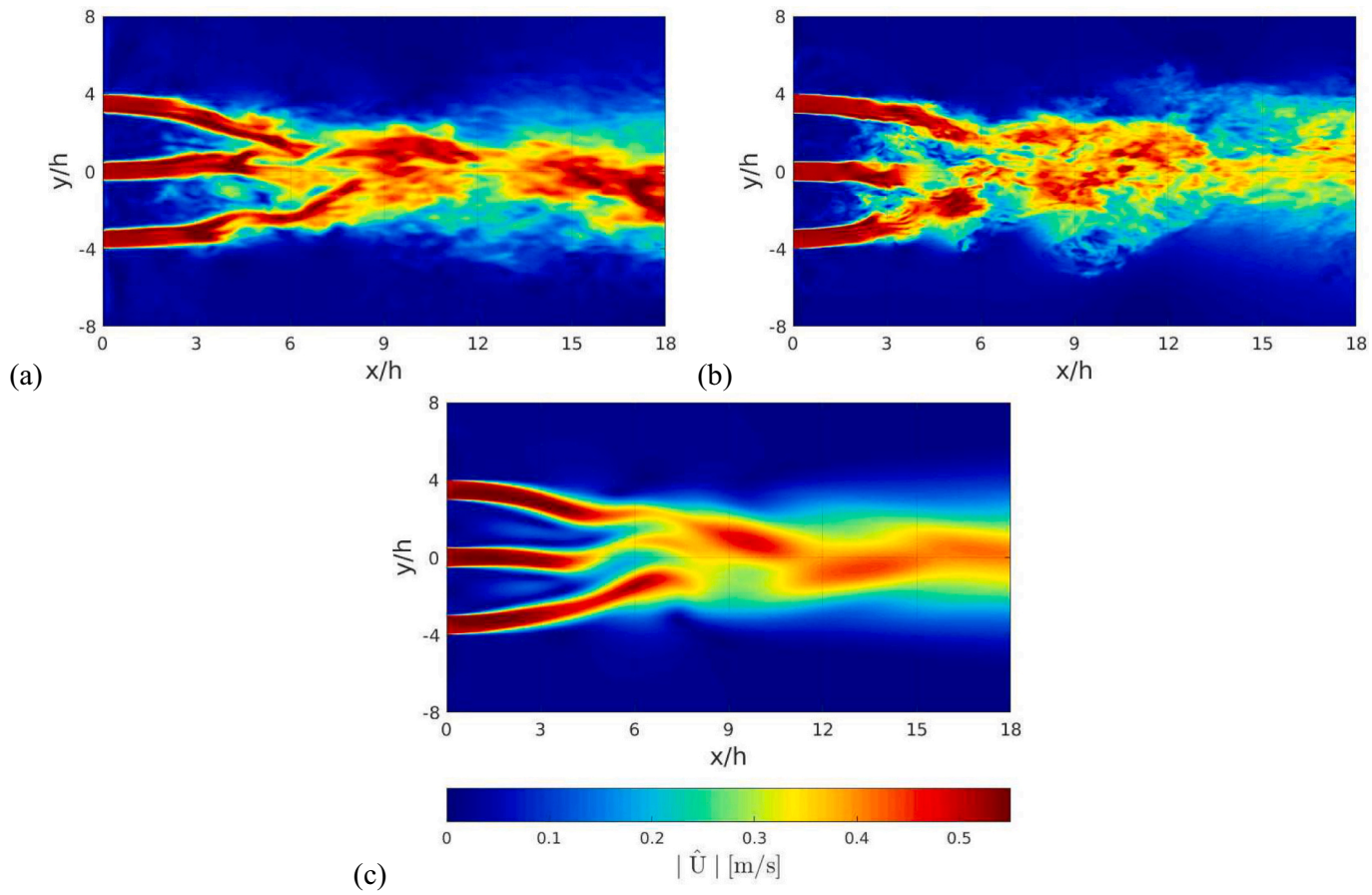

Fig. 5. Contours of instantaneous velocity magnitude in the central plane - data obtained from the coarse-mesh LES/DNS (a), fine-mesh LES/DNS (b) and T-RANS (c).

$$\frac{\partial \widehat{T}}{\partial t}+\frac{\partial \widehat{U}_j \widehat{T}}{\partial x_j}=\alpha\frac{\partial^2 \widehat{T}}{\partial x_j{}^2} \tag{3}$$

where ρ, ν and α are the molecular density, kinematic viscosity, and thermal diffusion, respectively. These are kept as constants in this study. For the LES technique, we set the spatial filter (denoted as'$\overline{\cdot}$' and related to cell size'Δ'), leading to the filtered momentum equation:

$$\frac{\partial \overline{U_i}}{\partial t}+\frac{\partial \overline{U_i}\,\overline{U_j}}{\partial x_j}=-\frac{1}{\rho}\frac{\partial \overline{p}}{\partial x_i}-\frac{\partial \tau_{ij}}{\partial x_j}+\nu\frac{\partial^2 \overline{U_i}}{\partial x_j{}^2} \tag{4}$$

where τ_{ij} is the SGS turbulent stress, which can be further indicated as:

$$\tau_{ij}=\overline{U_iU_j}-\overline{U_i}\;\overline{U_j} \tag{5}$$

and needs to be modeled, Pope [27]. Dealing with a low-Prandtl fluid, and in analogy with Cascioli et al. [16], we use a combined LES/DNS technique, which consists of the LES approach for the momentum transport (Eq.4) and DNS approach (full resolution, no SGS model) for the heat transport (Eq.3).

2.2. Dynamic subgrid-scale Smagorinsky model

The dynamic Smagorinsky SGS model allows the local calculation of the model coefficients, which are not fixed a priori, Germano et al. [28]. This is meant to improve the standard Smagorinsky SGS model, where a single and constant value of the Smagorinsky constant is set for the entire fluid domain, Smagorinsky [29]. A test grid (denoted with'$\widetilde{\cdot}$') is defined with a width of $\widetilde{\overline{\Delta}}=2\overline{\Delta}$. The subtest-tensor ($T_{ij}$) is then achieved as:

$$T_{ij}=\widetilde{\overline{U_iU_j}}-\widetilde{\overline{U_i}}\;\widetilde{\overline{U_j}} \tag{6}$$

It is shown in Germano et al. [28] that resolved stress can be expressed as:

$$L_{ij}=T_{ij}-\widetilde{\tau_{ij}} \tag{7}$$

and it can be explicitly evaluated from the large-scales as:

$$L_{ij}=\widetilde{\overline{U_i}\,\overline{U_j}}-\widetilde{\overline{U_i}}\;\widetilde{\overline{U_j}} \tag{8}$$

The same closure Smagorinsky model is applied for both the grid-filter and test-filter turbulent stress with an identical value of the model coefficient C_s, and it can be written as:

$$\tau_{ij}-\frac{1}{3}\delta_{ij}\tau_{kk}=-2C_s\overline{\Delta}^2|\overline{S}|\overline{S_{ij}} \tag{9}$$

$$T_{ij}-\frac{1}{3}\delta_{ij}T_{kk}=-2C_s\widetilde{\overline{\Delta}}^2|\widetilde{\overline{S}}|\widetilde{\overline{S_{ij}}} \tag{10}$$

$$\overline{S_{ij}}=\frac{1}{2}\left(\frac{\partial \overline{U_i}}{\partial x_j}+\frac{\partial \overline{U_j}}{\partial x_i}\right),\quad \widetilde{\overline{S_{ij}}}=\frac{1}{2}\left(\frac{\partial \widetilde{\overline{U_i}}}{\partial x_j}+\frac{\partial \widetilde{\overline{U_j}}}{\partial x_i}\right) \tag{11}$$

where C_s is the dynamic Smagorinsky constant (to be calculated over-time), while $\overline{S_{ij}}$ and $\widetilde{\overline{S_{ij}}}$ are the strain rate tensors calculated over the grid-filter $\overline{\Delta}$ and test-filter $\widetilde{\overline{\Delta}}$, respectively. Considering the Eqs.(10),(12) and (13), one obtains:

$$L_{ij}-\frac{1}{3}\delta_{ij}L_{kk}=2C_sM_{ij} \tag{12}$$

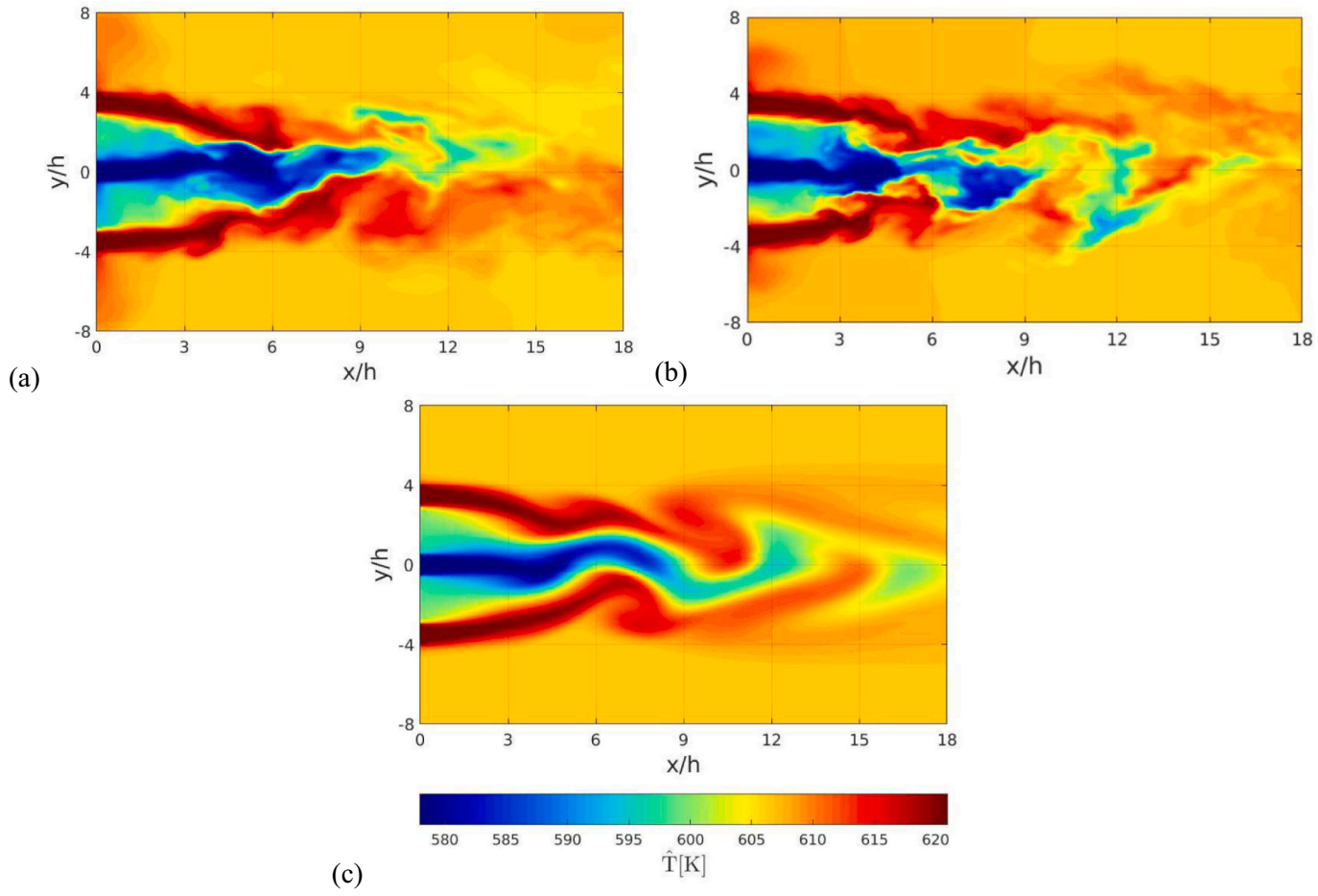

Fig. 6. Contours of instantaneous temperature in the central plane - data obtained from the coarse-mesh LES/DNS (a), fine-mesh LES/DNS (b) and T-RANS (c).

where

$$M_{ij} = \widetilde{\overline{\Delta}^2}|\widetilde{\overline{S}}|\widetilde{\overline{S}_{ij}} - \overline{\Delta}^2\widetilde{|\overline{S}|\overline{S}_{ij}} \tag{13}$$

We consider an adapted version of the original dynamic approach, as developed by Lilly [30], where a least squares method is applied to optimize the C_s value as:

$$(e_{ij})^2 = \left(L_{ij} - \frac{1}{3}\delta_{ij}L_{kk} - 2C_sM_{ij}\right)^2 \tag{14}$$

The turbulent SGS viscosity can be finally defined as:

$$\nu_{SGS} = C_s\overline{\Delta}^2|\overline{S}| \tag{15}$$

to close of the filtered momentum equation. In analogy with Cascioli et al. [16], we locally average C_s within the six "neighbor" cells, and bind the turbulent SGS viscosity ($\nu_{SGS} \geq -\nu$), to allow some backscattering, Righolt et al. [31,32].

2.3. T-RANS simulation

The time-dependent RANS (T-RANS) simulations were run considering constant-value fluid properties. The Reynolds-averaged transport equations are:

$$\frac{\partial U_i}{\partial t} + U_j\frac{\partial U_i}{\partial x_j} = -\frac{1}{\rho}\frac{\partial p}{\partial x_i} + \frac{\partial}{\partial x_j}\left[(\nu+\nu_t)\frac{\partial U_i}{\partial x_j}\right] \tag{16}$$

$$\frac{\partial T}{\partial t} + U_j\frac{\partial T}{\partial x_j} = \frac{\partial}{\partial x_j}\left[(\alpha+\alpha_t)\frac{\partial T}{\partial x_j}\right] \tag{17}$$

where ν_t is the turbulent viscosity and α_t is the turbulent thermal diffusivity, to be modeled. In analogy to Cascioli et al. [13], a four equation $k-\varepsilon-k_\theta-\varepsilon_\theta$ model is employed here, though not in its low-Reynolds variant. The original low-Reynolds modeling was introduced and further developed by Abe et al. [8], Hanjalić et al. [9], Manservisi and Menghini [10,11]. The transport equations are:

$$\frac{\partial k}{\partial t} + U_j\frac{\partial k}{\partial x_j} = P_k - \varepsilon + \frac{\partial}{\partial x_j}\left[\left(\nu+\frac{\nu_t}{\sigma_k}\right)\frac{\partial k}{\partial x_j}\right] \tag{18}$$

$$\frac{\partial \varepsilon}{\partial t} + U_j\frac{\partial \varepsilon}{\partial x_j} = (C_{\varepsilon_1}P_k - C_{\varepsilon_2}\varepsilon)\frac{\varepsilon}{k} + \frac{\partial}{\partial x_j}\left[\left(\nu+\frac{\nu_t}{\sigma_\varepsilon}\right)\frac{\partial \varepsilon}{\partial x_j}\right] \tag{19}$$

$$\frac{\partial k_\theta}{\partial t} + U_j\frac{\partial k_\theta}{\partial x_j} = \frac{\partial}{\partial x_j}\left[\left(\alpha+\frac{\alpha_t}{\sigma_{k_\theta}}\right)\frac{\partial k_\theta}{\partial x_j}\right] + P_\theta - \varepsilon_\theta \tag{20}$$

$$\begin{aligned}\frac{\partial \varepsilon_\theta}{\partial t} + U_j\frac{\partial \varepsilon_\theta}{\partial x_j} &= \frac{\partial}{\partial x_j}\left[\left(\alpha+\frac{\alpha_t}{\sigma_{\varepsilon_\theta}}\right)\frac{\partial \varepsilon_\theta}{\partial x_j}\right] \\ &+\frac{\varepsilon_\theta}{k_\theta}\left(C_{p_1}P_\theta - C_{d_1}\varepsilon_\theta\right) + \frac{\varepsilon_\theta}{k}\left(C_{p_2}P_k - C_{d_2}\varepsilon\right)\end{aligned} \tag{21}$$

where $P_k = \left[\nu_t\left(\frac{\partial U_i}{\partial x_j}+\frac{\partial U_j}{\partial x_i}\right) - \frac{2}{3}\delta_{ij}k\right]\frac{\partial U_i}{\partial x_j}$ and $P_\theta = \alpha_\theta\left(\frac{\partial T}{\partial x_j}\right)^2$ represent the modeled productions of turbulent kinetic energy and thermal fluctuations, respectively. The turbulent viscosity and turbulent thermal diffusivity can be defined as:

$$\nu_t = C_\mu\frac{k^2}{\varepsilon},\quad \alpha_t = C_\theta\frac{k^2}{\varepsilon}\frac{2R}{R+0.5} \tag{22}$$

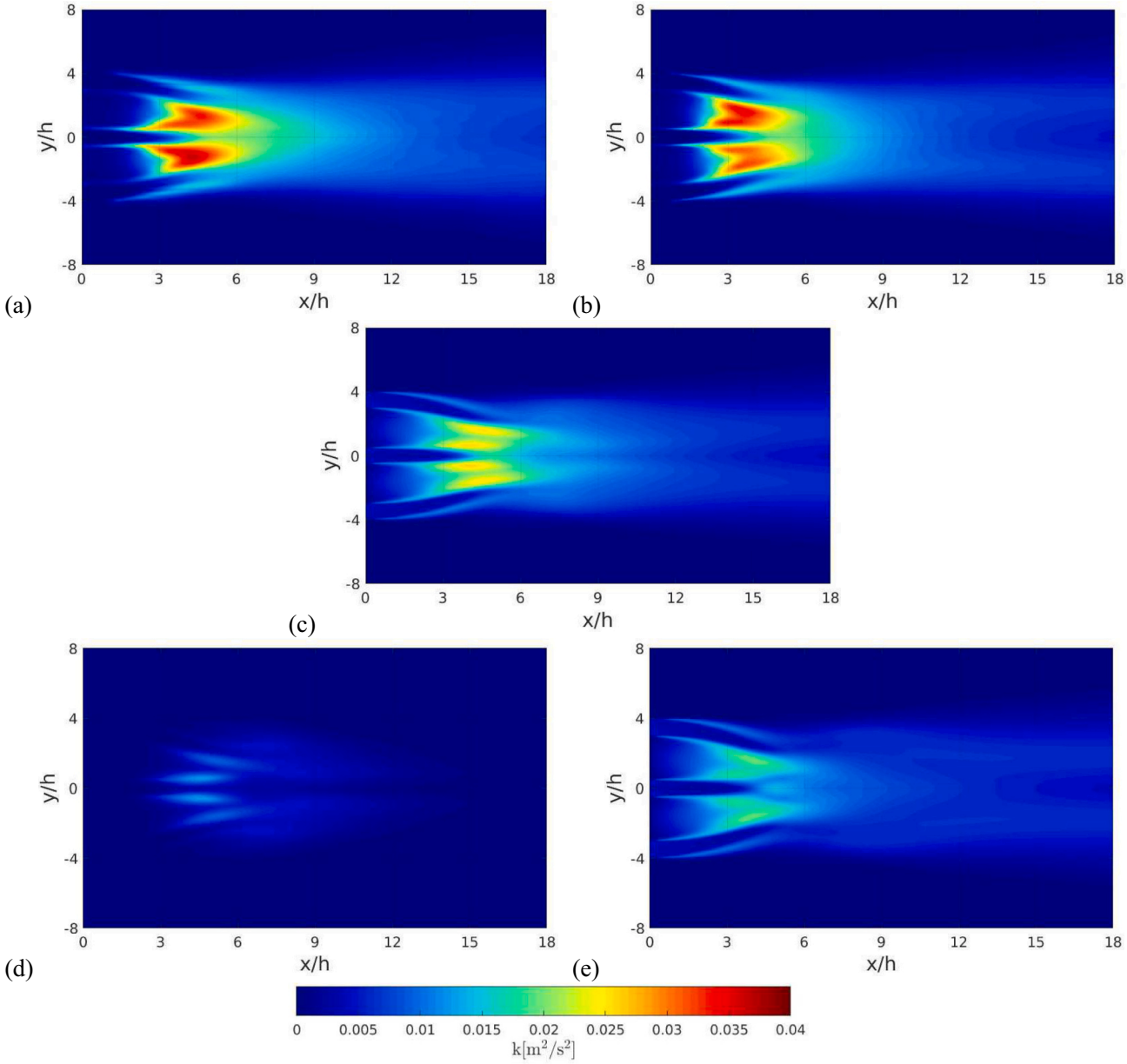

Fig. 7. Contours of the long-term time-averaged turbulent kinetic energy from the coarse-mesh LES/DNS (a), fine-mesh LES/DNS (b) and T-RANS (c). In addition, contours of the numerically resolved (d) and modeled (e) contributions to the T-RANS results (c).

where $R = \frac{\tau_\theta}{\tau_u} = \left(\frac{k_\theta}{\epsilon_\theta}\right) / \left(\frac{k}{\epsilon}\right)$ is the thermal to dynamical time scale ratio. All the model coefficients are collected in Table 1, Launder and Spalding [33], and Table 2, Manservisi and Menghini [11]. Note that no additional re-calibration of such model coefficients is being performed in the present study. The standard wall functions were used for the turbulence quantities along the no-slip walls.

2.4. Computational code

Both the LES/DNS and T-RANS simulations are performed by using the OpenFOAM CFD code (version 2.4.0). The dynamic Smagorinsky SGS model and ($k_\theta - \epsilon_\theta$) THT models were coded as additional new libraries, and validation is provided in the previous publications, Cascioli et al. [13,16]. To combine the velocity and pressure fields, the PISO algorithm was selected, Issa et al. [34]. For the LES/DNS, the gradient, Laplacian, and divergence terms were discretized by using a second-order central differencing scheme (CDS), while the second-order backward (implicit) scheme was used to integrate the time derivative term. The Courant number was kept below the value of 1.2, with an average value lower than the unity. In the case of T-RANS simulations, the cell-limited CDSs were used for the gradient and Laplacian terms, while second-order upwind schemes were used to discretize the divergence terms.

3. Computational details

3.1. Computational domain

The PLAJEST triple-jet experimental setup (a) and details of the inlet nozzles (b), are shown in Fig. 1, Kimura et al. [17,18] and Kobayashi et al. [19]. This triple-jet configuration consists of three parallel jets in a closed environment. The two side jets are characterized by the heated fluid at $T_H = 620.7$ K, while the central cold jet has an inlet temperature of $T_C = 577.5$ K. As mentioned, sodium is the working fluid (Pr = 0.006),

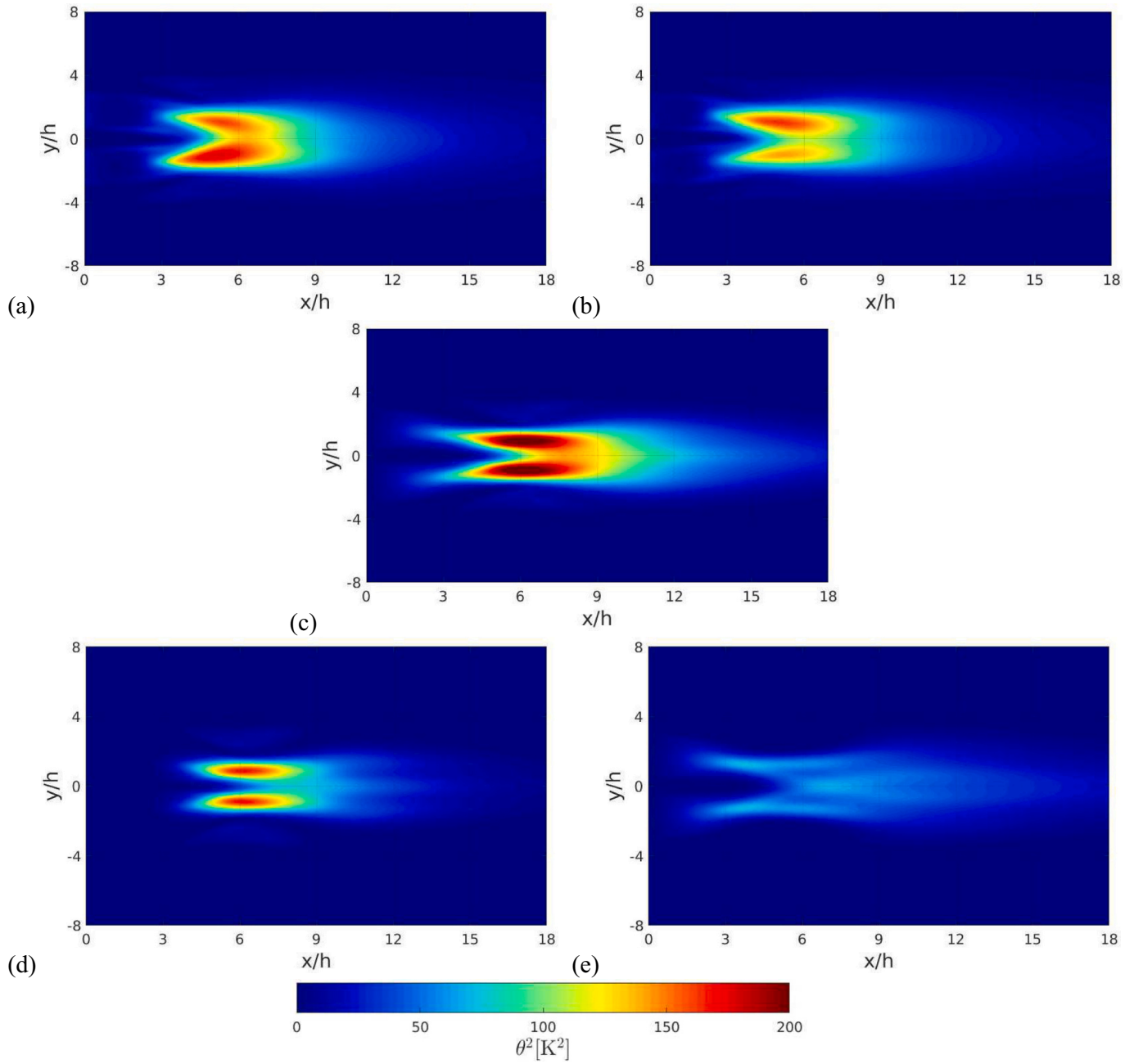

Fig. 8. Contours of the long-term time-averaged temperature variance from the coarse-mesh LES/DNS (a), fine-mesh LES/DNS (b) and T-RANS (c). In addition, contours of the numerically resolved (d) and modeled (e) contributions to the T-RANS results (c).

with a constant molecular kinematic viscosity of $\nu = 3.73{\cdot}10^{-7}$ m^2/s. Each nozzle has the same height, h = 0.02 m, corresponding to a Reynolds number of Re = 27,300. All other thermo-physical properties of the fluid are assumed as constants. Gravity effects are being neglected considering the forced convection regime, with a Richardson number of Ri $= 8.72{\cdot}10^{-3}$.

We have simulated two three-dimensional computational domains, Fig. 2. The LES/DNS simulations were performed on a simplified computational domain (three 0.5 h-long straight inlet channels), Fig. 2-left (domain A), whereas the T-RANS simulation domain also included realistic inlet nozzles, Fig. 2-right (domain B). The simplified domain (A) ensures a high mesh quality and affordable computational costs for the LES/DNS simulations. The numerical resolution in the spanwise direction (Δz^+) is important to achieve reliable performances when the periodic boundary conditions are projected at the simplified inlet planes for the LES/DNS simulations, Cascioli et al. [16]. Both domains are 5 h-wide in the spanwise direction. In both cases, despite the vertical orientation of the experimental facility, the coordinate system in our simulations was oriented with U, V, and W representing the velocity components in streamwise (x), crosswise (y) and spanwise (z) directions, respectively. The origin of the coordinate system (x = 0) is set at the interface between the central jet nozzle and the mixing domain.

3.1.1. *Domain A - LES/DNS*

For the LES/DNS simulations, domain A was imposed and two numerical resolutions were generated. The coarse numerical mesh (denoted as 'c-LES') contains about 2 million control volumes in the mixing region, whereas the fine numerical mesh (denoted as'f-LES') reaches 16 million control volumes. Details of both numerical meshes in the mixing region are given in Table 3. The mesh for the inlet channels is optimized

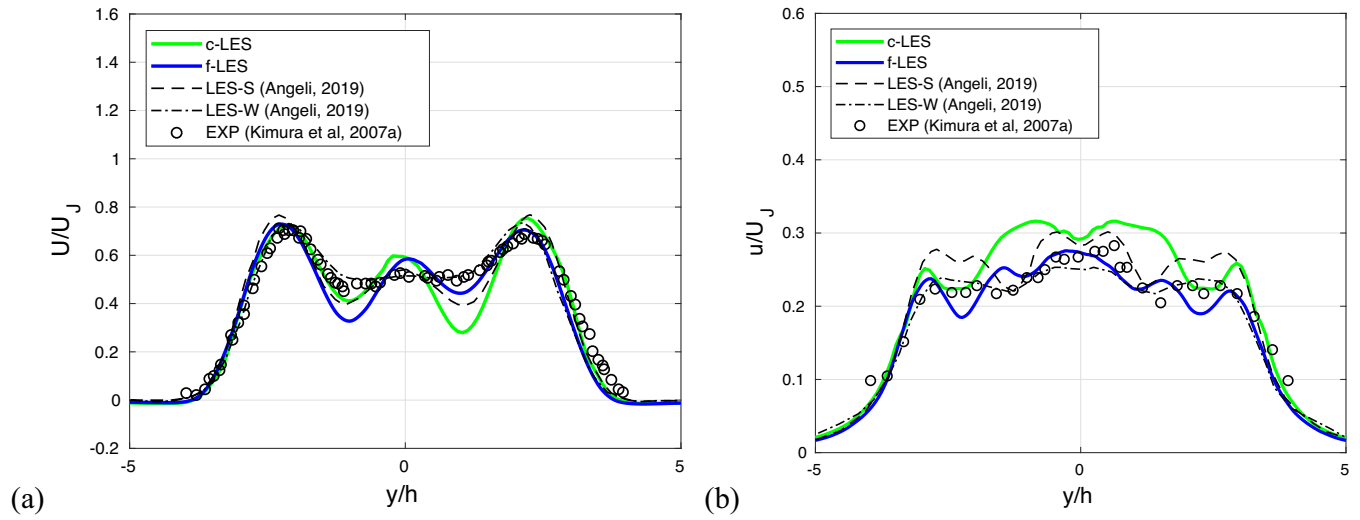

Fig. 9. Profiles of the mean non-dimensional streamwise velocity (U/U_J) (a) and fluctuating (u/U_J) (b) contributions at x/h = 5.

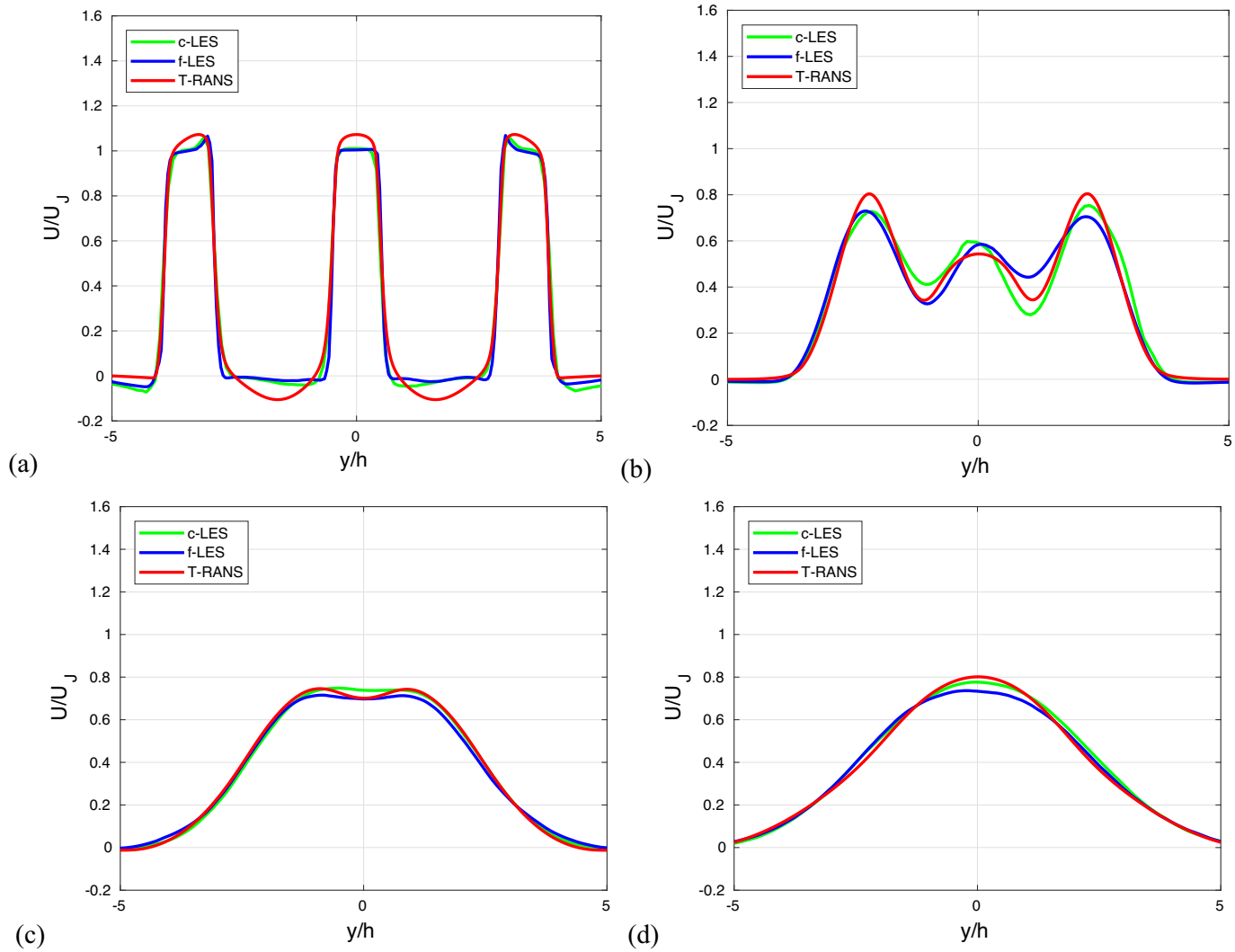

Fig. 10. Profiles of the non-dimensional mean streamwise velocity (U/U_J)) at different locations: x/h = 1, 5, 9, and 13 (a-d).

to ensure $y^+ < 1$. The maximum aspect ratio of 5.1 was imposed for both meshes. The initial velocity was set to zero, while the initial temperature was specified as an average between hot and cold jet temperature weighted with the corresponding mass flows. At the inlet patches of the channels, a uniform velocity (U_J) was set to (0.51, 0, 0) m/s. The no-slip velocity boundary condition was set at all walls, whereas the T_H and T_C

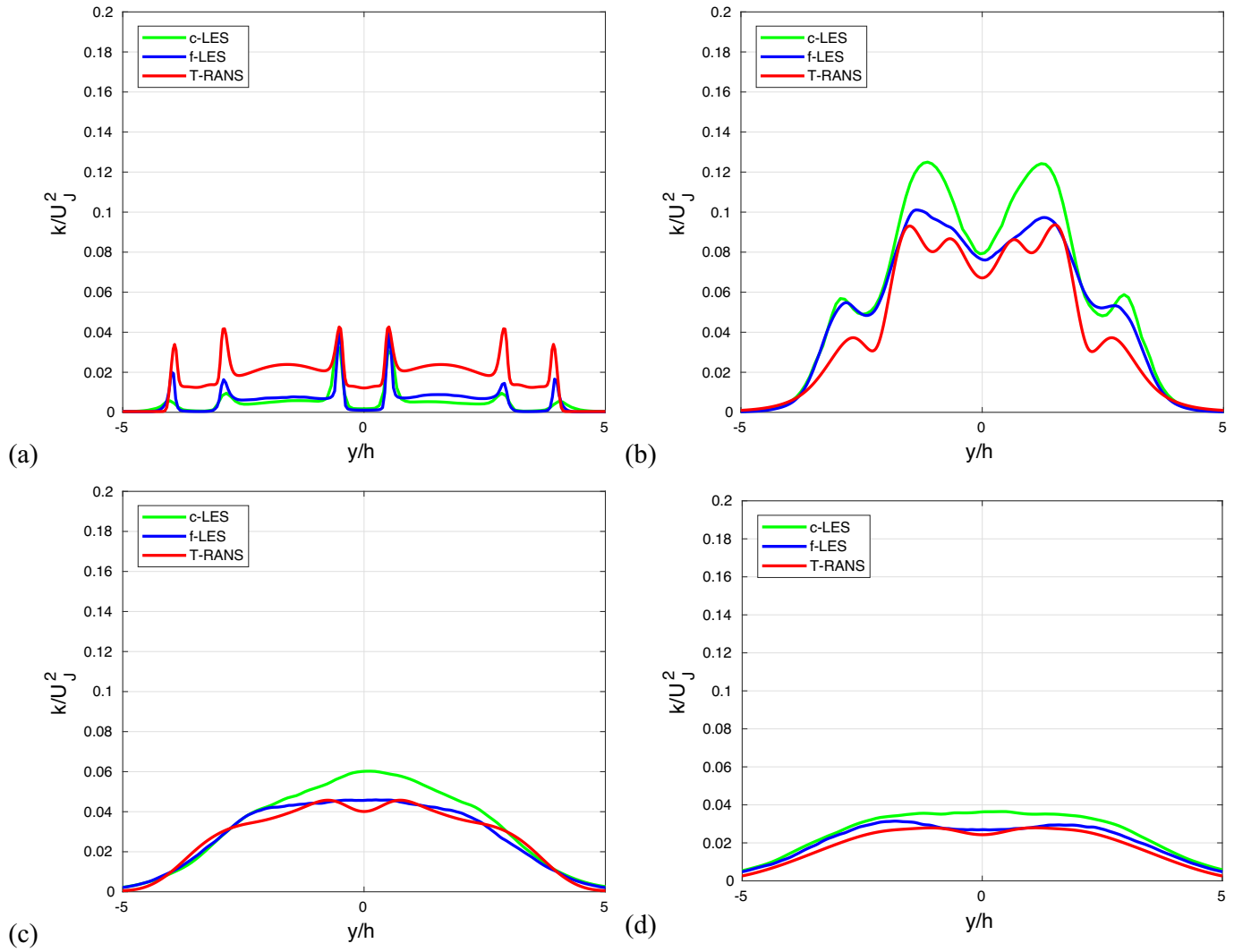

Fig. 11. Profiles of the normalized turbulent kinetic energy (k/U_j^2) at different locations: x/h = 1, 5, 9 and 13 (a-d).

values were set along the hot and cold channel walls, respectively. The walls between the nozzles are adiabatic. The pressure zero-gradient condition is imposed at the inlet patches and at the walls. Three openings (top, bottom, and end) are set in the mixing domain as outlet patches, with a modified zero-gradient boundary condition for velocity. It applies a zero-gradient condition to the flux out of the domain and calculates the inflow velocity based on a patch-normal flux. Here, the total pressure was calculated as $p_{out} = P_0 - \frac{1}{2}|U_{out}^2|$, where P_0 is the constant-value static pressure. In OpenFOAM, these boundaries are imposed through the application of the '*pressureInletOutletVelocity*' (for the velocity) and '*totalPressure*' (fore pressure) directives, which are recommended for the open atmosphere fluid domains. The zero-gradient of temperature was imposed at the outlet. Finally, the cyclic boundary conditions are applied for all spanwise-normal surfaces in the z-direction.

3.1.2. Domain B - T-RANS

Domain B was developed for the T-RANS simulation and mainly differs from domain A by the inlet channel modeling. The inlet channels are about 4.5 h-long and 3 h-high (before narrowing). Consequently, an inlet velocity (U_{in}) of (0.17, 0, 0) m/s was set at the inlet patches, in order to reach the same Reynolds number at the nozzle section as for the case of domain A. The minimum wall unit value along these channels is $y^+ = 12$. In order to represent the rounded sides of the experimental entrainment section, but to avoid the mesh singularities at the top and bottom corners of the mixing region, domain B is slightly extended (by 2 h) in the cross-flow direction as compared to domain A. The final mesh was characterized by a maximum cell aspect ratio of 24.3, maximum cell non-orthogonality of 51.1 (particularly in the rounded corner regions), and maximum skewness of 0.61. The total (including inlet and mixing regions) number of control volumes is about 1.4 million, where additional details of the numerical mesh are given in Table 3. The initial and boundary conditions for velocity and temperature are analogous to those of domain A. Additional initial and boundary conditions need to be specified for turbulence quantities of the four-equation ($k - \varepsilon - k_\theta - \varepsilon_\theta$) model. For all turbulence variables, a zero-gradient boundary condition is imposed at the outlets, whereas the symmetry boundary condition is imposed for the front and back of the simulation domain (i.e. in the z-coordinate direction). It should be noted that in the original experimental configuration a test plate was placed along one side of the rectangular jets, which is not simulated in the present study. We kept identical spanwise extension for both domains A and B of 5 h, to clarify the role of the inlet nozzles shape. At the inlet, the turbulence intensity (I_t) of 10% was identified after a parametric study (on a two-dimensional configuration) to achieve the optimal value and get a good agreement with the experimental data. Then, the inlet turbulence kinetic energy and its dissipation rate were calculated as: $k = \frac{3}{2}(U_{in}I_t)^2$ and $\varepsilon = C_\mu^{3/4}\frac{k^{3/2}}{0.07H}$, with $H = 3h$. The inlet thermal variance and its

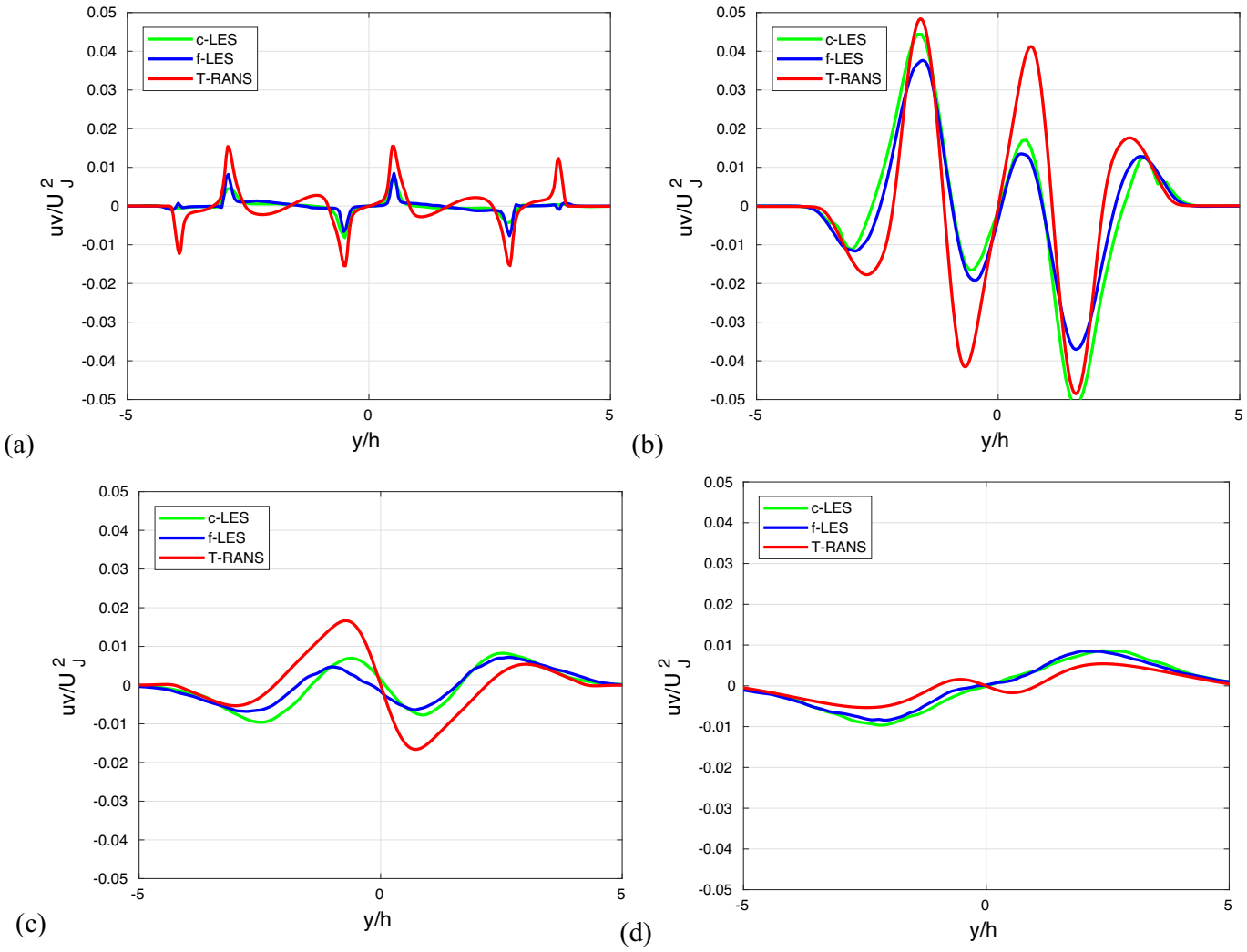

Fig. 12. Profiles of normalized turbulent shear-stress component (uv/U_J^2) at different locations: x/h = 1, 5, 9 and 13 (a-d).

dissipation rate were both specified as $k_\theta = \epsilon_\theta = 0$. Along the walls, the wall functions were imposed for the turbulence kinetic energy and its dissipation rate. For the thermal field turbulence, the following conditions were imposed: $k_\theta^{wall} = 0$ and $\varepsilon_\theta^{wall} = 2\alpha\left(\frac{k_\theta}{\Delta y_n^2}\right)_{(wall-1)}$, where Δy_n is the distance between the wall and the nearest cell center.

3.1.3. Characteristic length scales for LES/DNS

To ensure the appropriate resolution of the computational mesh, the characteristic Kolmogorov and Corrsin length scales are estimated in accordance to Ruiz-Chavarria et al. [35], as:

$$\eta = \left(\frac{\nu^3}{\epsilon}\right)^{\frac{1}{4}}, \quad \eta_\theta = \eta\, Pr^{-\frac{3}{4}} \tag{23}$$

The dissipation rate was calculated and averaged ($\langle \ldots \rangle$) in runtime as: $\epsilon = \nu\left\langle \left(\frac{\partial u_i'}{\partial x_j}\right)^2 \right\rangle$, with $u_i' = \widehat{U}_i - \langle U_i \rangle$. In analogy to Cascioli et al. [16], a qualitative assessment of the mesh resolution can be performed by plotting the ratios between the characteristic cell length ($l_c = (\Delta_{CV})^{1/3} = (\Delta x \cdot \Delta y \cdot \Delta z)^{1/3}$) over η and η_θ, as shown by Fig. 3 concerning the coarser LES/DNS. Fig. 3(a) relates to the velocity field, we can see that the coarse numerical mesh resulted in a l_c/η ratio of 30 in the shear regions between the central and side jets, indicating that even finer mesh needs to be employed in order to have a well-resolved LES. We observed a reduced range of a l_c/η ratio of 5–10 in the case of the finer LES/DNS. In contrast, the ratio of l_c/η_θ is showing that temperature field is well-resolved even with the coarser mesh, Fig. 3(b).

4. Results

4.1. Qualitative analysis of the flow and thermal fields

To provide insights into a three-dimensional structure of the parallel triple-jet of sodium, we plot isovolumes of the vorticity magnitude (15–45 Hz), colored by instantaneous velocity and temperature, respectively, Figs.4(a), (b). These structures are plotted for the LES with the fine numerical mesh. The process of merging and mixing of the central and side jets is clearly illustrated. The contours of the magnitude of the instantaneous velocity in the central streamwise plane for the coarse-mesh LES, fine-mesh LES, and T-RANS simulations are shown in Fig. 5. Distinct imprints of the three jets can be seen in the proximity of the inlet plane followed by a formation of the central mixing region. As expected, the fine mesh LES/DNS (Fig. 5(b)), shows the flow in the greatest detail, where T-RANS provides a rather smooth distribution, Fig. 5(c). The contours of the instantaneous temperature in the central plane for three simulations are shown in Fig. 6. The imprints of the three jets are again visible in the proximity of the inlet. In contrast to the velocity structures, the presented temperature fields show more diffusive structures, due to the considered low-Prandtl value.

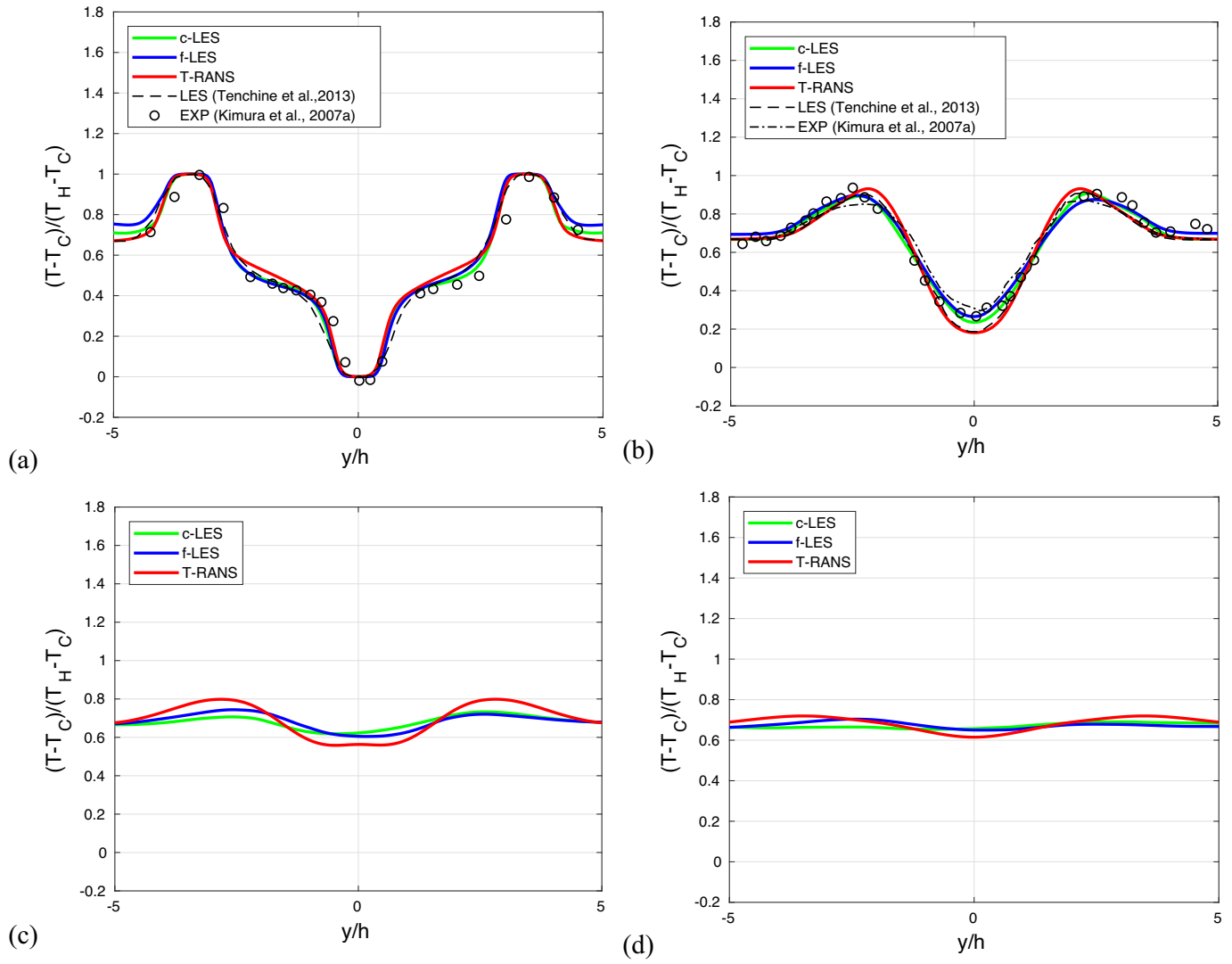

Fig. 13. Profiles of the normalized long-term time-averaged temperature profiles at different locations: x/h = 1, 5, 9 and 13 (a-d).

The contours of the long-term time-averaged turbulent kinetic energy obtained with different simulation techniques in the central plane are shown in Figs.7 (a), (b), (c). For all simulations, two distinct peaks of the turbulent kinetic energy at the start of the triple-jet mixing region can be observed together with dominant shear regions between the jets. The characteristic peak values are similar for the coarse- (Fig. 7(a)) and fine-LES (Figs.7(b)), whereas T-RANS values are slightly lower, Fig. 7(c). Furthermore, the streamwise extension (i.e. x/h = 9) of the regions characterized by high values of the turbulent kinetic energy is similar for all the presented simulation techniques. For the T-RANS, the total turbulent kinetic energy was split into the numerically resolved (Fig. 7(d)) and modeled (Fig. 7(e)) contributions, i.e. $k_{tot} = k_{res} + k_{mod}$, $k_{res} = \frac{1}{2}\overline{(u_i' u_i')}$, $k_{mod} = \text{PDE}(k)$, where PDE is the partial differential equation Eq.(19)). It can be seen that for the T-RANS approach the modeled contribution is dominant and that numerically resolved contributions are confined to the central mixing region, i.e. up to x/h = 15.

Contours of the time-averaged temperature variance in the central plane are shown in Fig. 8. For both coarse- (Fig. 8(a)) and fine-mesh (Fig. 8(b)) LES/DNS approach contours show slightly asymmetrical distributions, which is a consequence of the shorter duration of the long-term time-averaging procedure (due to limited computational resources). In contrast, the T-RANS results exhibit a fully symmetrical distribution, Fig. 8(c). For all simulation techniques, two characteristic peaks are observed, and in contrast to the turbulent kinetic energy, the T-RANS shows higher peaks in comparison to the LES/DNS. The total contribution of temperature variance is again split into the numerically resolved and modeled contributions, i.e. $(k_\theta)_{tot} = (k_\theta)_{res} + (k_\theta)_{mod}$, $(k_\theta)_{res} = \frac{1}{2}\overline{(\theta'\theta')}$, $k_{mod} = \text{PDE}(k_\theta)$, Eq.(22)). It can be seen that now the numerically resolved contribution is larger than its modeled counterpart, Figs.8(d) and (e). It is interesting to note that the resolved contribution shows small values up to x/h = 4, where the modeled contribution dominates. In contrast, between x/h = 4 and x/h = 9, the resolved contribution dominates.

4.2. Quantitative analysis of the flow field

Next, we move to perform a comparative assessment of the simulated velocity field with available measurements and/or simulations from the literature. The long-term time-averaging was performed for all simulation techniques and the statistically convergent results were obtained for 24 (T-RANS), 85 (coarse-mesh LES/DNS) and 128 (fine-mesh LES/DNS) Flow-Through-Times (FTTs), respectively. The FTT was defined as the time required by the massless fluid particle to move from the inlet to the outlet of the mixing domain at the constant jet velocity U_J, giving approximately a FTT of 1.18 s for both simulated domains.

The non-dimensional profiles of the mean and fluctuating streamwise velocity component at x/h = 5 are shown in Figs.9(a) and (b),

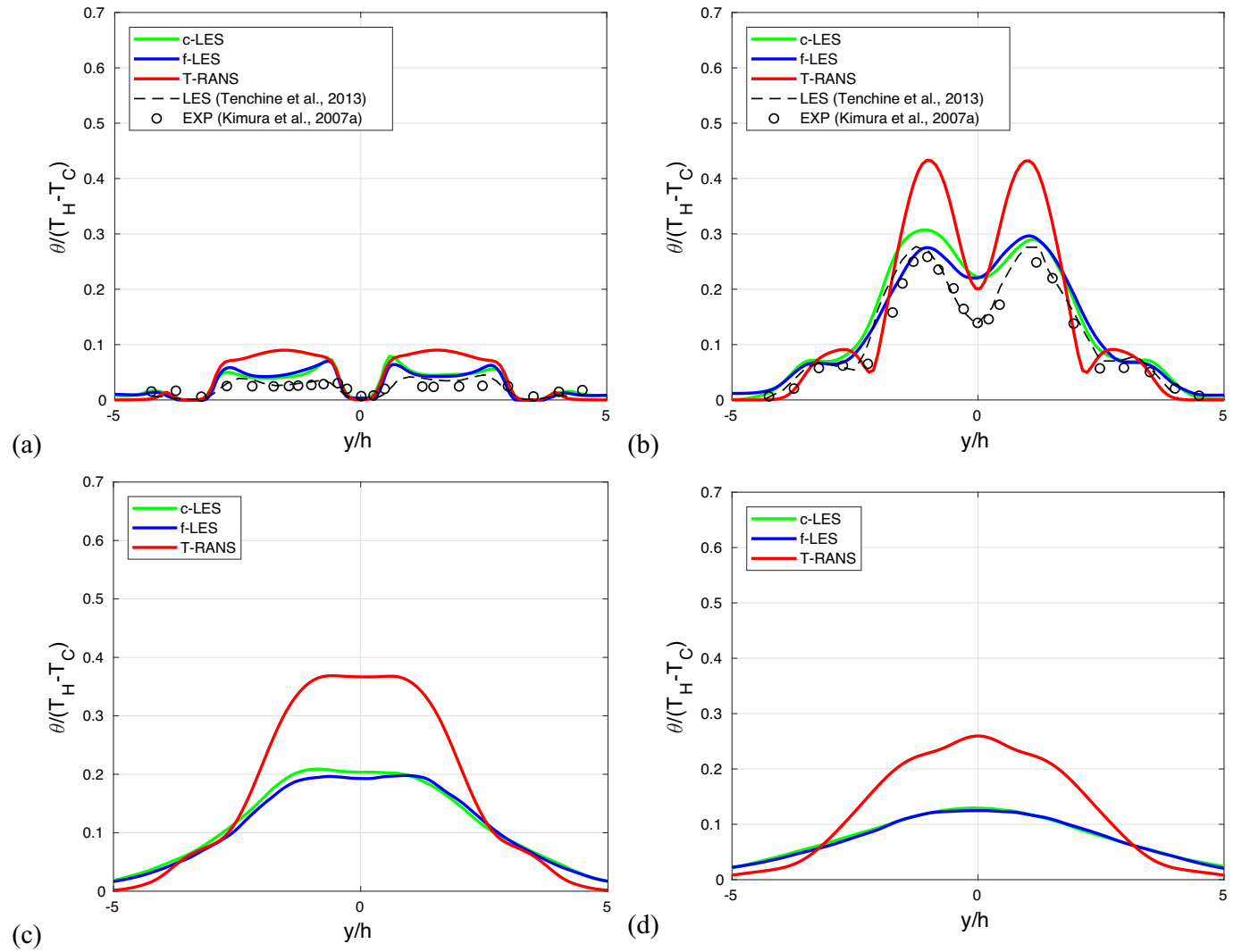

Fig. 14. Profiles of the non-dimensional temperature fluctuations ($\theta^*_{rms} = \theta/(T_H - T_C)$) at different locations: x/h = 1, 5, 9 and 13 (a-d).

respectively. The profiles of the mean streamwise velocity exhibit good agreement with the experimental data of Kimura et al. [17] (extracted from [22]), and LES results of Angeli [22] obtained with two different SGS closures: the standard Smagorinsky (denoted as LES-S) and the WALE (denoted as LES-W) models. The results shown for comparison with the present results are for the finest mesh of [22], which contained about $8.7{\cdot}10^6$ elements with an average ratio $\Delta/\eta_k = 21$, which is similar to our numerical simulations with the coarse-LES approach. The peaks and outer regions are well captured with the fine-mesh LES/DNS, whereas a slight asymmetry is visible in the central region, Fig. 9(a). The slight asymmetry is also visible in the experimental data and LES-W of Angeli [22], although the present simulations indicate smaller values in the inner region. This asymmetry can be attributed to the very long-time persisting flipping behavior of the central jet that can require a much longer time-averaging procedure, which was not computationally affordable. The profiles of the non-dimensional fluctuating streamwise component at the same location x/h = 5 show particularly good agreement with the present fine-mesh LES, as shown in Fig. 9(b).

A comparative assessment of the mean streamwise velocity profiles with results of the present simulations at various locations x/h = 1, 5, 9, and 13, is shown in Fig. 10. Close to the inlet plane, i.e. x/h = 1, the coarse- and fine-mesh LES show a good agreement, while the T-RANS produces slightly larger peak values of the jets and larger negative values between the central and side jets, indicating a stronger backflow here, Fig. 10(a). At x/h = 5 (already previously addressed regarding comparison with our LES and results from the literature), a relatively good agreement between the present T-RANS and LES results is obtained, where the T-RANS profiles exhibit a fully symmetrical distribution and peaks are slightly overestimated. At farther downstream locations, x/h = 9 and x/h = 13, the distinct triple-jet imprint is not visible anymore confirming an efficient mixing of the side and central jets, Figs.10(c) and (d). For these locations, an overall very good agreement is observed between various simulation techniques.

The profiles of the non-dimensional turbulent kinetic energy (k/U_J^2) at identical locations are shown in Fig. 11. Close to the inlet location, at x/h = 1, the T-RANS shows higher levels of turbulence compared to the coarse-mesh and fine-mesh LESs, Fig. 11(a). The latter have a good overlap except at the edge of the outer zone, where the peak shear location is underpredicted by the coarse-mesh LES. In contrast, all simulations are showing a good agreement in peak values of the turbulent kinetic energy at the central jet shear zones. At x/h = 5 location, the coarse-mesh LES overpredicts the fine-mesh LES in the central region, Fig. 11(b). The T-RANS profiles exhibit characteristic 6-peak behavior, indicating a slower merging of the side- and central jet. In the central region, the peak values of T-RANS are slightly underpredicted in comparison with the fine-mesh LES. Farther downstream, at x/h = 9 location, the peak values of T-RANS show a very good agreement with the fine-mesh LES, despite having a less established mixing

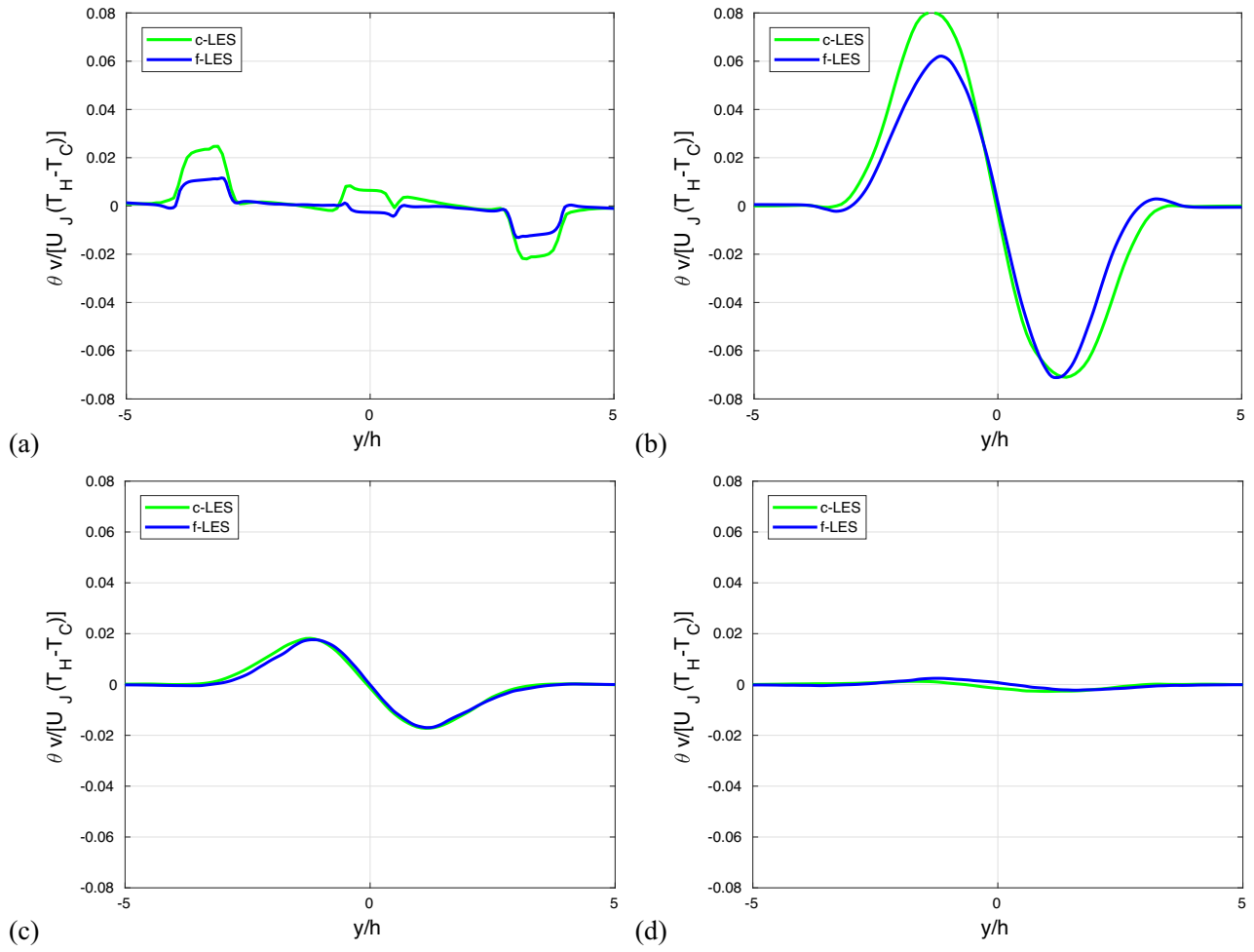

Fig. 15. Profiles of the normalized vertical component of the turbulent heat flux $(\theta v/U_J(T_H - T_C))$ at the different locations: x/h = 1, 5, 9 and 13 (a-d).

(indicated by a presence of two little peaks around the center-line), Fig. 11(c). At the same location, the coarse-mesh LES is showing a single peak behavior, but with its peak value overpredicting the fine-mesh LES. Finally, at x/h = 13, differences between simulations are smaller, and the coarse-mesh LES are again overpredicting the center-line value, Fig. 11(d).

The profiles of the non-dimensional turbulent shear-stress component (uv/U_j^2) at the same locations are presented in Fig. 12. The T-RANS overpredicts the peak values in comparison with both the coarse-mesh and fine-mesh LESs at x/h = 1 location, Fig. 12(a). At location x/h = 5, the agreement between the coarse-mesh and fine-mesh LES is generally good, with an overprediction of the coarse-mesh LES in the central region, Fig. 12(b). Here, the T-RANS profile overpredicts the peak values. This trend of T-RANS overprediction is also visible at the x/h = 9 location, albeit with outer peaks now closer to the LES values, Fig. 12(c). At x/h = 15, the coarse- and fine-mesh LES show good mutual agreement, while the T-RANS profile is now underestimating the outer peak values, Fig. 12(d).

4.3. Quantitative analysis of the thermal field

The non-dimensional mean temperature profiles obtained with the presented simulations are compared with experiments of Kimura et al. [17,18] and LES of Tenchine et al. [20] at x/h = 1 and 5, are shown in Figs.13(a) and (b). The current LES/DNS results are in very good agreement with experiments at both locations, and they are showing some improvements at the x/h = 5 location in comparison with LES of [20]. The present T-RANS results also show an overall good agreement with experiments with some deviations in the central region at x/h = 5 location, Fig. 13(b). At x/h = 9, the T-RANS overpredicts the side-jet peaks, whereas the central region is underpredicted, Fig. 13(c). Finally, at x/h = 13, a good overlap is obtained among the various simulation techniques, Fig. 13(d).

The normalized temperature fluctuations profiles are shown in Fig. 14. Close to the inlet, current LESs are showing overprediction with respect to the experimental data, Fig. 14(a). The agreement is better at x/h = 5, where the peak values are well predicted, while the centerline value is still overpredicted, Fig. 14(b). Farther downstream, both coarse- and fine-mesh LES/DNSs are showing a good overlap, and a transition from the double- to single-peak behavior is observed, Figs.14(c), (d). In contrast to the present LES/DNS results, the agreement of thermal fluctuation profiles from T-RANS simulation with experiments is less satisfactory at x/h = 1 and 5. A significant overprediction is obtained at these and remaining locations indicating that further refinements of the $k_\theta - \varepsilon_\theta$ model are necessary. The overestimation indicates a too-weak dissipation of the temperature fluctuations. A first step in improving T-RANS simulations could be to increase contribution of the source terms in the transport equation of ε_θ, Eq.(23), but this further optimization and model recalibration are outside of the scope of the present work.

The profiles of the non-dimensional vertical component of the turbulent heat flux calculated with the coarse- and fine-mesh LES/DNSs are shown in Fig. 15. A good agreement is obtained for the larger distances from the inlet (at x/h = 9 and 13, Figs.15(c), (d)). Closer to the inlet, the coarse-mesh overestimates the fine-mesh LES results at both x/h = 1 and 5, Figs.15(a), (b). This discrepancy can be due to already observed

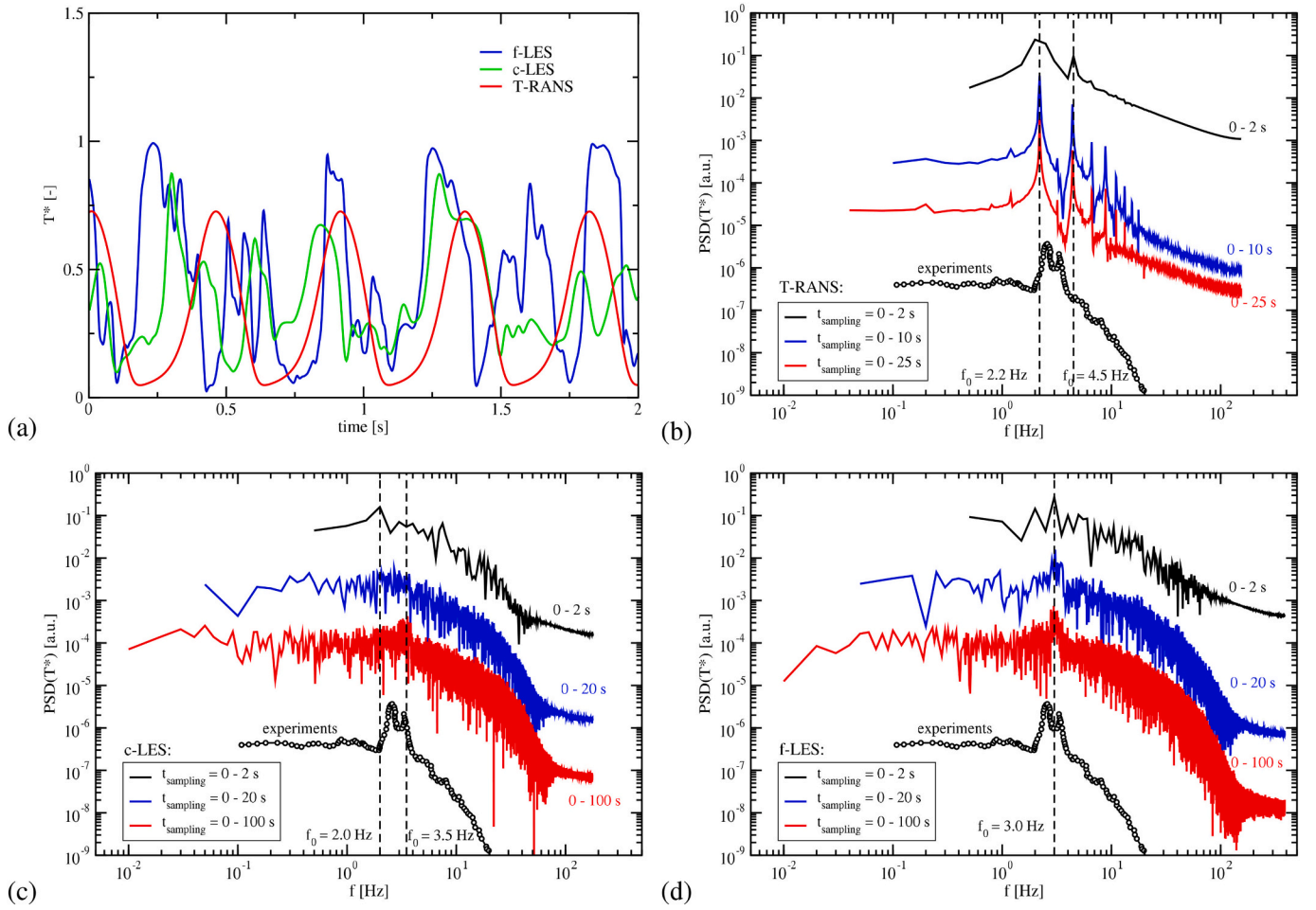

Fig. 16. Time series (a) and PSD distributions of non-dimensional temperature fluctuations ($T^* = (T - T_C)/(T_H - T_C)$) in the central plane at x/h = 5 and y/h = 0.75 from T-RANS (b), coarse-mesh LES (c) and fine-mesh LES (d) - comparison with experimental data of Kimura et al. [18]. Note that plots are systematically shifted vertically by factor 10^{-2} for a sake of readability.

turbulent kinetic energy differences between the coarse- and fine-mesh LES results at these locations.

4.4. Frequency-based power spectra

In addition to the already discussed instantaneous and time-averaged flow and thermal features, we focus on the monitoring of the time-dependent evolution of the temperature at the following location in the central plane (z/h = 0): x/h = 5, y/h = 0.75. This location is selected in order to make a comparison with thermocouple measurements performed by Kimura et al. [17,18]. The experimental studies of Kimura et al. [18] used thermocouples with an accuracy of 0.1 °C and time constant of approximately 20 ms. The measured temperature signal contained 20,000 samples with an interval of $\Delta t = 0.01$ s.

The characteristic time-series of the non-dimensional temperature signal ($T^* = (T - T_C)/(T_H - T_C)$) at the given monitoring location for the three simulations are shown in Fig. 16(a). The oscillatory behavior with a periodic signal indicates the presence of the Kelvin-Helmholtz instabilities triggered by the strong shear between the hot side jets and cold central jet. Note that for the sake of clarity, a short time interval of 2 s was shown. It can be seen that the T-RANS signal exhibits a perfectly periodic behavior when compared to the coarse- and fine-mesh LES. Furthermore, the amplitude of the T-RANS signal oscillations is fixed around $T^* = 0.75$. The PSD distributions for various simulation techniques are then analyzed. In experimental studies, a reduced temperature data set of 1024 samples and a time length of 10.24 s was extracted from the entire measured data of 200 s, and a Gaussian filter was applied. In total 200 data sets were generated by shifting the data array by one second in the total measured data. Then, the extracted data sets were converted by applying the Discrete Fourier Transform (DFT) and the final PSD was obtained by averaging all 200 FFT data sets. In conclusion, the authors mentioned that they have observed a prominent frequency component in their PSD distribution, but without any additional details.

In the present study, we followed a simpler approach in calculating the PSD of the temperature time series, as shown in Cascioli et al. [16], Kenjereš [36], Li et al. [37]. For each time signal, we performed analysis over three different time lengths, which were varying from 2 to 25 s for T-RANS, and from 2 s to 100 s for coarse- and fine-mesh LES. Note that a shorter time length for T-RANS (with a maximum of 25 s) was chosen because of its significantly faster statistical convergence when compared to the LES approach. Then, the DFT was calculated for each time length, and the final PSD was plotted and compared with experiments (where experimental data were extracted from plots in Fig. 5 in Kimura et al. [18]). The final PSD distributions $E_\theta(f) = \frac{1}{2}\theta'\theta'$ (where $\theta' = \widehat{T} - \langle\overline{T}\rangle$) are then systematically shifted vertically by factor 10^{-2} for a sake of readability.

The PSD distributions obtained with T-RANS data for three different time length intervals are shown in Fig. 16(b). Independently of the time length interval, the T-RANS captures the leading frequency $f_0 = 2.2$ Hz and consecutive doubling frequency harmonics. The leading frequency is in a reasonable agreement with the experimental data with $f_0 = 2.6$

Hz. The T-RANS distributions do not show a proper slope of the dissipative part of the spectra even for the longest time span, indicating that only the vortex-shedding frequency is captured. Note that here we made an analogy with the spatial spectra since the highest frequencies are also associated with the largest wave numbers that correspond to the smallest length-scales present in the flow, and similarly, the lowest frequencies are associated with the largest flow length-scales, Arpaci and Larsen [38]. In contrast to the T-RANS, the coarse- and fine-mesh LES results properly capture slopes of both inertial and dissipative regions, Fig. 16(c), (d). In the case of the coarse-mesh LES, the short time length (0–2 s) predicts the single peak frequency around $f_0 = 2$ Hz, Fig. 16(c). With a further increase of time length, a shifted leading frequency of $f_0 = 3.5$ Hz is captured for the longest time length (0–100 s), which is in close agreement with the second experimental peak ($f_0 = 3.3$ Hz). The fine-mesh LES shows a consistent tendency to capture the single peak frequency of $f_0 = 3$ Hz for all considered time length intervals, Fig. 16(d). Both LES results show well-convergent predictions of the inertial and dissipative regions of the spectra for intermediate and long-time length intervals. The reported LES results are in good agreement with the LES of Tenchine et al. [20] who applied WALE subgrid closure and a simplified computational domain (similar to our domain A), and also captured the single critical frequency around 3 Hz. It can be concluded that the T-RANS simulation reasonably predicted the first dominant characteristic frequency even for the rather short time length interval of just 2 s, but it was not able to capture the proper slope of the dissipation region of the PSD distribution. In contrast, the fine-mesh LES consistently predicted the leading frequency in good agreement with the experimental second frequency and proper slopes of the inertial and dissipative regions of the spectra.

5. Summary and conclusions

In the present study, we performed combined dynamic wall-resolved LES / DNS of the forced convection low-Prandtl triple-jet configuration that represents the PLAJEST experiments of [17,18]. The first- and second-moments of the velocity and temperature were extracted at characteristic locations in the central plane at different distances from the inlet plane and were compared with available experimental data at particular locations. Furthermore, we also performed the T-RANS simulations with the high Reynolds variant (i.e. wall-functions approach) of the four-equation ($k-\varepsilon-k_\theta-\varepsilon_\theta$) model, which does not require a priori specification of Pr_t.

The non-dimensional mean streamwise velocity profiles at different locations from the inlet obtained with coarse-, fine-mesh LES / DNS, and T-RANS showed a good agreement. The profiles of non-dimensional turbulent kinetic energy at the same locations showed a good agreement between the fine-mesh LES / DNS and T-RANS, whereas the coarse-mesh LES / DNS results were overpredicted in the central mixing region.

The non-dimensional mean temperature profiles also showed a good agreement between all presented numerical simulation techniques and available experimental data. The profiles of the non-dimensional temperature variance demonstrated a good agreement between the coarse- and fine-mesh LES / DNS, while the T-RANS exhibited a significant overprediction.

The PSD analysis of the temperature signal demonstrated the ability of the applied T-RANS approach to capture the leading frequency in a reasonable agreement with experiments even for very short lengths of the time interval. The coarse-mesh LES / DNS was much more sensitive to a change in the length of the time interval. In contrast, the fine-mesh LES / DNS captured the leading frequency independently of the length of the time interval. Both coarse- and fine-mesh LES / DNS results demonstrated the existence of the inertial and dissipative regions of the spectra. The dissipation regime was not present in the spectra of the T-RANS approach, demonstrating its inability to capture the instabilities of the smaller flow structures. Despite this, especially from the perspective of industrial-scale applications, the T-RANS approach, with an improved version of the high-Reynolds variant of the four-equation ($k-\varepsilon-k_\theta-\varepsilon_\theta$) model, can be an interesting alternative to the computationally more demanding LES/DNS technique.

Results of the high-fidelity fine-mesh LES / DNS, especially regarding the temperature variance and turbulent heat flux profiles can be used for further improvement and recalibration of T-RANS models for low-Prandtl fluids. Since accurate information on temperature fluctuations (its amplitude and frequency) are prerequisite for predictions of thermal fatigue that can occur in the mixing jet regions (and potentially cause thermal striping and cracks), the wall-resolving dynamic LES / DNS approach is recommended.

CRediT authorship contribution statement

E. Cascioli: Writing – review & editing, Writing – original draft, Visualization, Validation, Software, Methodology, Formal analysis. **B. Kaaks:** Validation, Software, Formal analysis, Data curation. **S. Keijers:** Writing – original draft, Supervision. **K. Van Tichelen:** Writing – original draft, Supervision, Project administration, Funding acquisition. **S. Kenjereš:** Writing – review & editing, Writing – original draft, Visualization, Supervision, Resources, Project administration, Methodology, Investigation, Funding acquisition, Data curation, Conceptualization.

Declaration of competing interest

None Declared.

Data availability

Data will be made available on request.

Acknowledgment

This work was supported by European Commission's H2020-EURATOM program under Grants 654935 (SESAME) and 662186 (MYRTE).

References

[1] B.S. Triplett, E.P. Loewen, B.J. Dooies, PRISM: a competitive small modular sodium-cooled reactor, Nucl. Technol. 178 (2012) 186–200.
[2] S.L. Soloviev, D.G. Zaryugin, S.G. Kalyakin, S.T. Leskin, Identifying the key development areas for small nuclear power plants, Nuclear Energy Technol. 8 (2) (2022) 115–120.
[3] K. Van Tichelen, G. Kennedy, F. Mirelli, A. Marino, A. Toti, D. Rozzia, E. Cascioli, S. Keijers, P. Planquart, Advanced liquid-metal thermal-hydraulic research for MYRRHA, Nucl. Technol. 206 (2020) 150–163.
[4] G. Grötzbach, Challenges in low-Prandtl number heat transfer simulation and modelling, Nucl. Eng. Des. 264 (2013) 41–55.
[5] A. Shams, F. Roelofs, E. Baglietto, S. Lardeau, S. Kenjeres, Assessment and calibration of an algebraic turbulent heat flux model for low-Prandtl fluids, Int. J. Heat Mass Transf. 79 (2014) 589–601.
[6] F. Roelofs, A. Shams, I. Otic, M. Böttcher, M. Duponcheel, Y. Bartosiewicz, D. Lakehal, E. Baglietto, S. Lardeau, X. Cheng, Status and perspective of turbulence heat transfer modelling for the industrial application of liquid metal flows, Nucl. Eng. Des. 290 (2015) 99–106.
[7] W.M. Kays, Turbulent Prandtl number - where are we? J. Heat Transf. 116 (1994) 284–295.
[8] K. Abe, T. Kondoh, Y. Nagano, A new turbulence model for predicting fluid flow and heat transfer in separating and reattaching flows - II. Thermal calculations, Int. J. Heat Mass Transf. 38 (8) (1995) 1467–1481.
[9] K. Hanjalić, S. Kenjereš, F. Durst, Natural convection in partitioned two-dimensional enclosures at higher Rayleigh numbers, Int. J. Heat Mass Transf. 39 (7) (1996) 1407–1427.
[10] S. Manservisi, F. Menghini, A CFD four parameter heat transfer turbulence model for engineering applications in heavy liquid metals, Int. J. Heat Mass Transf. 69 (2014) 312–326.
[11] S. Manservisi, F. Menghini, CFD simulations in heavy liquid metal flows for square lattice bare rod bundle geometries with a four parameter heat transfer turbulence model, Nucl. Eng. Des. 295 (2015) 251–260.
[12] R. Da Viá, S. Manservisi, F. Menghini, A $k-\Omega-k_\theta-\Omega_\theta$ four parameter logarithmic turbulence model for liquid metals, Nucl. Eng. Des. 101 (2016) 1030–1041.

[13] E. Cascioli, S. Buckingham, S. Keijers, K. Van Tichelen, S. Kenjereš, Numerical and experimental analysis of a planar jet with heated co-flow at medium and low Prandtl-number values, Nucl. Eng. Des. 361 (2020) 110570.
[14] A. De Santis, A. Shams, Application of an algebraic turbulent heat flux model to a backward facing step flow at low Prandtl number, Ann. Nucl. Energy 117 (2018) 32–44.
[15] A. De Santis, A. Villa Ortiz, A. Shams, L. Koloszar, Modelling of a planar impinging jet at unity, moderate and low Prandtl number: assessment of advanced RANS closures, Ann. Nucl. Energy 129 (2019) 125–145.
[16] E. Cascioli, S. Keijers, K. Van Tichelen, J.E. Vesper, S. Kenjereš, Combined large-Eddy and Direct numerical simulations of a planar jet with heated co-flow with medium and low Prandtl fluids, Int. J. Heat Mass Transf. 191 (2022) 122774.
[17] N. Kimura, H. Kamide, P. Emonot, K. Nagasawa, Study on Thermal Striping Phenomena in Triple-Parallel Jet – Investigation on Non-Stationary Heat Transfer Characteristics Based on Numerical Simulation, Proceedings of 12th International Topical Meeting on Nuclear Reactor Thermal Hydraulics (NURETH-12), Pittsburgh, USA, 2007.
[18] N. Kimura, H. Miyakoshi, H. Kamide, Experimental investigation on transfer characteristics of temperature fluctuation from liquid sodium to wall in parallel triple-jet, Int. J. Heat Mass Transf. 50 (2007) 2024–2036.
[19] J. Kobayashi, M. Tanaka, S. Ohno, H. Ohshima, H. Kamide, Proposal of Benchmark Problem of Thermal Striping Phenomena in Planar Triple Parallel Jets Tests for Fundamental Code Validation in Sodium-Cooled Fast Reactor Development, Proceedings of 16th International Topical Meeting on Nuclear Reactor Thermal Hydraulics (NURETH-16), Chicago, IL, USA, 2015.
[20] D. Tenchine, S. Vandroux, V. Barthel, O. Cioni, Experimental and numerical studies on mixing jets for sodium cooled fast reactors, Nucl. Eng. Des. 263 (2013) 263–272.
[21] F. Nicoud, F. Ducros, Subgrid-scale stress modelling based on the square of the velocity gradient tensor, Flow, Turbul. Combust. 62 (13) (1999) 183–200.
[22] P.E. Angeli, Verification and validation of LES of a triple parallel jet flow in the context of a thermal striping investigation, Nucl. Eng. Des. 353 (2019) 110210.
[23] S. Kenjereš, K. Hanjalić, Transient analysis of Rayleigh-Bénard convection with a RANS model, Int. J. Heat Fluid Flow 20 (3) (1999) 329–340.
[24] S. Kenjereš, K. Hanjalić, LES, T-RANS and hybrid simulations of thermal convection at high Ra numbers, Int. J. Heat Fluid Flow 27 (5) (2006) 800–810.
[25] S. Kenjereš, K. Hanjalić, Tackling complex turbulent flows with transient TRANS, Fluid Dynam. Res. 41 (2009) 012201.
[26] M. Nishimura, A. Tokuhiro, N. Kimura, H. Kamide, Numerical study on mixing of oscillating quasi-planar jets with low Reynolds number turbulent stress and heat flux equation models, Nucl. Eng. Des. 202 (1) (2000) 77–95.
[27] S.B. Pope, Turbulent Flows, Cambridge University - Cambridge Univ. Press, 2000.
[28] M. Germano, U. Piomelli, P. Moin, W.H. Cabot, A dynamic subgrid-scale eddy viscosity model, Phys. Fluids A 3 (1991) 1760–1765.
[29] J. Smagorinsky, General circulation experiments with the primitive equations. I. The basic experiment, Mon. Weather Rev. 91 (1963) 99–164.
[30] D.K. Lilly, A proposed modification of the Germano subgrid-scale turbulence closure method, Phys. Fluids A 4 (1992) 633–635.
[31] B.W. Righolt, S. Kenjereš, R. Kalter, M.J. Tummers, C.R. Kleijn, Dynamics of an oscillating turbulent jet in a confined cavity, Phys. Fluids 27 (2015) 1–16.
[32] B.W. Righolt, S. Kenjereš, R. Kalter, M.J. Tummers, C.R. Kleijn, Electromagnetic control of an oscillating turbulent jet in a confined cavity, Int. J. Heat Fluid Flow 62 (2016) 395–406.
[33] B.E. Launder, D.B. Spalding, The numerical computation of turbulent flows, Comput. Methods Appl. Mech. Eng. 3 (1973) 269–289.
[34] R.I. Issa, A.D. Gosman, A.P. Watkins, The computation of compressible and incompressible recirculating flows by a non-iterative implicit scheme, J. Comput. Phys. 62 (1986) 66–82.
[35] G. Ruiz-Chavarria, C. Baudet, S. Ciliberto, Scaling laws and dissipation scale of a passive scalar in fully developed turbulence, Phys. D 99 (1996) 380–396.
[36] S. Kenjereš, Energy spectra and turbulence generation in the wake of magnetic obstacles, Phys. Fluids 24 (11) (2012) 115111.
[37] H. Li, N.K. Anand, Y.A. Hassan, T. Nguyen, Large eddy simulations of the turbulent flows of twin parallel jets, Int. J. Heat Mass Transf. 129 (2019) 1263–1273.
[38] V.S. Arpaci, P.S. Larsen, Convection Heat Transfer, Prentice-Hall, Inc., New Jersey, USA, 1984.